UNIVERSIDAD DE CHILE
FACULTAD DE CIENCIAS FÍSICAS Y MATEMÁTICAS
DEPARTAMENTO DE GEOFÍSICA

HYDROGEOPHYSICAL CHARACTERIZATION OF THE VIÑA DEL MAR BOTANICAL GARDEN WATERSHED

TESIS PARA OPTAR AL GRADO DE MAGÍSTER EN CIENCIAS, MENCIÓN GEOFÍSICA

BORJA FARAH CELIS

PROFESOR GUÍA:
Daniel Díaz Alvarado

PROFESOR CO-GUÍA:
Juvenal Letelier Villalón

MIEMBROS DE LA COMISIÓN:
Andrei Maksymowicz Jeria
Ana Prieto Santa

Este trabajo ha sido financiado por:
Centro CAPTA y el Departamento de Geofísica de la Universidad de Chile.

SANTIAGO DE CHILE
2024

CARACTERIZACIÓN HIDROGEOFÍSICA DE LA CUENCA DEL JARDÍN BOTÁNICO DE VIÑA DEL MAR

La hidrogeofísica es una sub-disciplina de la geofísica que se ocupa de estudiar la geometría y la dinámica de los sistemas de agua subterránea. Durante las últimas décadas, ha ganado importancia debido a la posibilidad de complementar observaciones directas.

El Jardín Botánico de Viña del Mar (JBVM) está ubicado dentro de una cuenca de 7.5 km^2, en la Cordillera de la Costa, entre las ciudades de Viña del Mar y Quipué, en la región de Valparaíso, Chile. Dada la presencia de un estero perenne y una laguna artificial, ha sido indentificada como zona de interés por el consorcio de investigación Centro Avanzado para Tecnologías del Agua (CAPTA), con el objetivo de implementar nuevas tecnologías para tratamiento de aguas. Con esta motivación, se realizó este estudio geofísico para entender la geohidrología de esta área.

Los métodos utilizados fueron tomografía de resistividad eléctrica (ERT por su sigla en inglés), transiente electromagnético (TEM) y gravimetría. El objetivo de esta campaña geofísica fue estimar el nivel freático y la profundidad de basamento, así como delimitar zonas preferenciales para la recarga artificial del acuífero.

Los resultados obtenidos sugieren una geología dominada por la presencia de roca fracturada en torno al JBVM, como se observa en cuencas intramontanas similares (San Martín, 2023). Combinando los resultados de los tres métodos, la zona de estudio puede ser caracterizada por cuatro estructuras: sedimento no consolidado, basamento altamente fracturado, basamento normal (2670 km/m^3 de densidad) y basamento de alta densidad. El nivel freático fue estimado entre 1 y 6 metros de profundidad en toda el área de estudio. El basamento de alta densidad podría corresponder a un cuerpo, y el basamento fracturado forma dos posibles lineamientos que se alinean con las fallas mapeadas en la zona. Se propone que los depocentros son la mejor opción para realizar la recarga artificial de los acuíferos.

HYDROGEOPHYSICAL CHARACTERIZATION OF THE VIÑA DEL MAR BOTANICAL GARDEN WATERSHED

Hydrogeophyisics is the sub-discipline of geophysics that concerns about the understanding of the geometry and dynamics of groundwater systems. It has gained importance in the last decade due to the possibility to compliment direct observations in a cheaper and less time-consuming manner. Even though this sub-discipline is widely used, there are not many academic articles that apply it in Chile. In this context, the present work consists in one of the few articles that uses geophysics as its main data source to study a watershed located in Chile.

The Botanical Garden of *Viña del Mar* is located inside a 7.5 km^2 watershed in the Coastal Cordillera, between the cities of *Quilpué* and *Viña del Mar*, in the *Varparaíso* Region in *Chile*. Due to the presence of a perennial stream and an artificial lagoon, this area has gained the interest of the research consortium *Centro Avanzado para Tecnologías del Agua* (CAPTA), with the goal of implementing water treatment technologies. With this motivation, a geophysical study was done to understand its underlying geohydrology.

The methods used were electrical resistivity tomography (ERT), transient electromagnetic (TEM) and gravimetry. The aim of this geophysical survey was to estimate the groundwater depth and the basement thickness, as well as delimit possible preferential areas for artificial aquifer recharge.

The results suggest a geology dominated by the presence of fractured rock surrounding the VMBG, as seen in similar intramontane basins (San Martín, 2023). Combining the results from the three methods, the study area can be characterized by four features: unconsolidated sediment, highly fractured basement, normal (2670 km/m^3 density) basement, and high density basement. The water table depth was estimated between 1 and 6 meters in all the studied area. The high density basement could correspond to one body, and the fractured basement forms two lineaments that align with the mapped faults in the study area. It is proposed that the depocenters are the best option to perform the aquifer recharge.

DEDICATORIA

Y volveremos a ver
En este juego tan simple
De emocionarse con cosas que no son notadas
En los contornos de un globo que gira en silencio. Eduardo Gatti

AGRADECIMIENTOS

Agradecimientos

En primer lugar, quisiera agradecer al centro de Investigación CAPTA y al departamento de Geofísica de la Universidad de Chile por su financiamiento y hacer todo esto posible, al profesor Daniel Díaz por su apoyo y sus consejos, y al profesor Juvenal Letelier por confiar en mí para realizar este trabajo. Quisiera también agradecer a quienes participaron de las campañas de terreno, Hernán, Pablo y Rafael. Gracias a los y las académicas que no participan formalmente de este trabajo, pero que me dieron consejos y apoyo fundamental: Bertrand Potin, Bárbara Blanco y Francisco Ortega. Gracias además al Núcleo de Geofísica Aplicada y a Sergio Contreras y Luis Villegas por sus indispensables consejos y ayuda.

Decir que esta tesis es un logro individual sería una mentira. A toda mi familia, muchas gracias por apoyarme siempre, y por darme el espacio y la tranquilidad para poder estudiar. Gracias a la Amanda, por cuidarme y por quererme. Gracias a Claudia Reyes, y gracias a Eugenio Marcos por crear un refugio donde compartir la tristeza, la alegría y el cariño. A mis amigos del alma, Raimundo, Martín y Ignacio, gracias por estar siempre, especialmente en los momentos más difíciles. A todes les cabres de la selección de escalada de la Universidad de Chile, gracias por las risas y por hacer más ameno este difícil proceso.

Por último, a Vicente, no hay palabras para agradecerte todo lo que me has enseñado. A pesar de ya no estar, te llevo conmigo en cada lugar y en cada momento. Esta tesis es para ti.

Table of Content

List of Tables

List of Figures

Chapter 1

Introduction

In the context of mega-drought in central Chile (Garreaud et al., 2017, 2020; Boisier et al., 2016), understanding groundwater resources and minimizing the cost and impact associated appears as a national necessity. Geophysics has emerged during the last decades as a way to complement direct observations (eg. wells) (Binley et al., 2015; Robinson et al., 2008) in order to thoroughly study and understand groundwater systems. In Chile, some of the recent hydrogeophysical works include the study of the interaction between the granular aquifer and fractured rocks in San Felipe-Los Andes (Taucare et al., 2020; Figueroa et al., 2021), Catemu intramontane basin (Martín, 2023) located in the Valparaiso region and Parque Nacional Río Clarillo (Marti et al., 2023). These works compliment the geophysica data with other types of information, such as geochemistry and field observations.

The present work is a hydrogeophysical study of a watershed located in the Valparaíso Region, in central Chile, the Botanical Garden of *Viña del Mar* (BGVM) is found inside this watershed. Only two works were found that study this area. The first is the geological map of the Valparaíso-Curacaví at a 1:100.000 scale (de Geología y Minería et al., 1996). The other work is the geology thesis of Felipe Lopeguetiz, which consists in a numeric hydrogeological model, based on soil humidity measurements, electrical resistivity tomography, and seismic refraction. Besides these works, the other available information is a well where the water table was at 5.4 meters in may 2022, and the water conductivity measured in three different parts of the stream in september 2020. The values obtained were 1219, 864 and 876 μS/cm.

1.1. Motivation and objectives

This work is part of the research center *Centro Avanzado para Tecnologías de Agua* (CAPTA). This center is a consortium of *Universidad de Chile*, *Universidad de Playa Ancha* and *Universidad de Atacama*, that aims to provide technologic alternatives to increase the national hydrology portfolio. More specifically, this research is part of the project P3 of CAPTA, that has as objective to develop new water treatment technologies, to treat greywaters and then inject the treated water into aquifers for long-term storage.

The BGVM stands out as a zone of interest for this project for many reasons, as is further explained in section 3.2. The BGVM is situated in central Chile, a region that has experienced a mega drought since 2010 (Garreaud et al., 2017), and the Valparaíso Commune where the BGVM is located was declared a hydric stressed area by the Chilean Water Directorate

(DGA), as can be seen in their web page. The comparatively small size of the watershed (its area is 7.5 km^2) makes it possible to perform a detailed research more easily than in bigger basins. There is an artificial lagoon in the BGVM, that makes it an ideal location to study surface water-groundwater interactions. Furthermore, this zone was chosen by CAPTA to use an artificial wetland as a biofilter. Thus, and considering the interest of CAPTA for this zone, this thesis is proposed as the first work to understand the groundwater geometry in the BGVM, necessary for the realization of future hydrologic or hydrogeologic works.

The objectives are divided in general and specific. The general objective is to define the geometry of the aquifer present in the study zone. The specific objectives are:

- Identify the phreatic level in the study area, based on the resistivity structure of the ground.
- Define the basement geometry, using a density model calculated from a surface gravity anomaly.
- Delimit ideal zones for artifitial aquifer recharge.

Chapter 2

Methodology

2.1. Rock resistivity

The electrical resistivity of rocks is a property that depends on factors such as the mineralogical constitution, distribution and amount of porosity, degree of fluid saturation (eg. gas, water) and temperature (Samouëlian et al. (2005) and references therein). The range of values for this parameter varies between 10^0 and 10^5 [Ωm] (Figure 2.1).

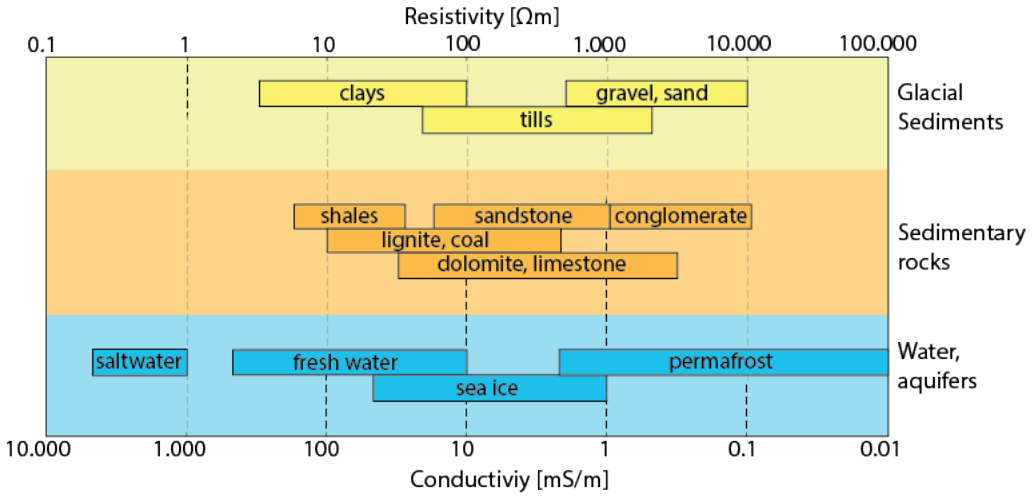

Figure 2.1: Resistivity ranges of different types of rocks and water. Modified from Samouëlian et al. (2005)

Rocks or sediments can have porosity, open space within it that can be empty (filled with air) or retain fluid, usually water, but also natural gas and oil. The content of water (or other fluid) contained in a material is a determining factor of its electrical resistivity. This dependence is described by an empirical relation (Archie, 1942), showed in equation 2.1. Clay minerals present a difficulty in terms of electrical resistivity interpretation. Due to its high ion exchange capacity, clay tends to form what its called an electrical double layer of exchange of cations, the first layer is fixed and adjacent to the clay, but the second layer is diffuse an can move when an electrical field is applied, thus increasing the surface conductivity (Ward, 1990). Because of this mechanism, when saturated, clay can have resistivities as low as 1 [Ωm], and can be mistakenly interpreted as an aquifer.

$$\rho = \rho_w \cdot a\phi^{-m} \tag{2.1}$$

In the equation shown above, ρ_w is the electrical resistivity contained in the pores, a and m are constants related with the saturation coefficient and degree of cementation respectively, and ϕ is the porosity. Figure 2.2 shows the dependence of resistivity on the amount of water, for clay.

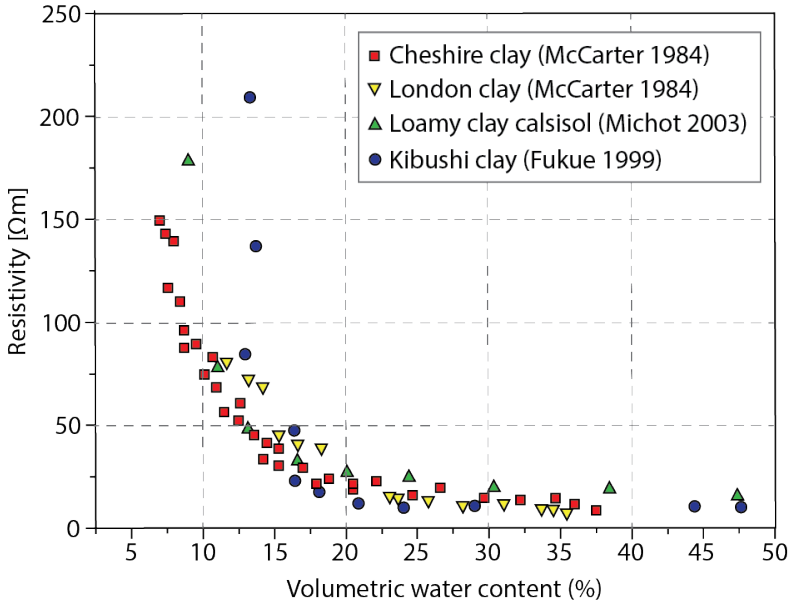

Figure 2.2: Relation between volumetric water content and resistivity, modified from Samouëlian et al. (2005)

Due to this dependence, geophysical methods that infer electrical resistivity (such as electric and some electromagnetic methods) are widely used in groundwater research (Binley et al., 2015). Many authors thus use geophysical techniques that result in resistivity models to study problems such as buried sediments that potentially host aquifers (Danielsen et al., 2003) groundwater-surface water interaction (Albouy et al., 2001), freshwater aquifer-saltwater aquifer interaction (Johnson et al., 2012) and soil moisture estimation (Brunet et al., 2010; Miller et al., 2008).

2.2. Rock density

The density, that is, the mass per unit of volume, changes importantly between different earth materials. The two main parameters that determine the density of an earth material, are the composition and the porosity. The porosity is particularly important in sedimentary rocks and unconsolidated sediments, the fraction of air contained plays and important role in the density of the whole material, referred to as bulk density. Furthermore, if the material is saturated in a fluid, commonly water, the density will also change. It is then useful to define two different densities, dry bulk density, shown in equation (2.2) and saturated bulk density, shown in equation (2.3).

$$\rho_b = \frac{W_g}{V_b} \tag{2.2}$$

$$\rho_s = \frac{W_g + (V_p \rho_w)}{V_b} \tag{2.3}$$

In these two equations, W_g is the weight of the grains, V_b is the bulk volume, V_p is the interconnected pore volume and ρ_w is the water density.

Even if the density of minerals can be measured accurately, the density of a certain rock will depend on its composition. For this reason, all rock densities have a range of possible values, according to the fraction of the different minerals composing it. The mathematical expression of this is shown in equation 2.4, where C_i and ρ_i are the volumetric fraction and density of the i^{th} mineral.

$$\rho_b = C_1 \cdot \rho_1 + C_2 \cdot \rho_2 + ... + C_n \cdot \rho_n \tag{2.4}$$

The density ranges of rocks and sediments concerning this work were collected from different publications, and are summarized in Figure 2.3.

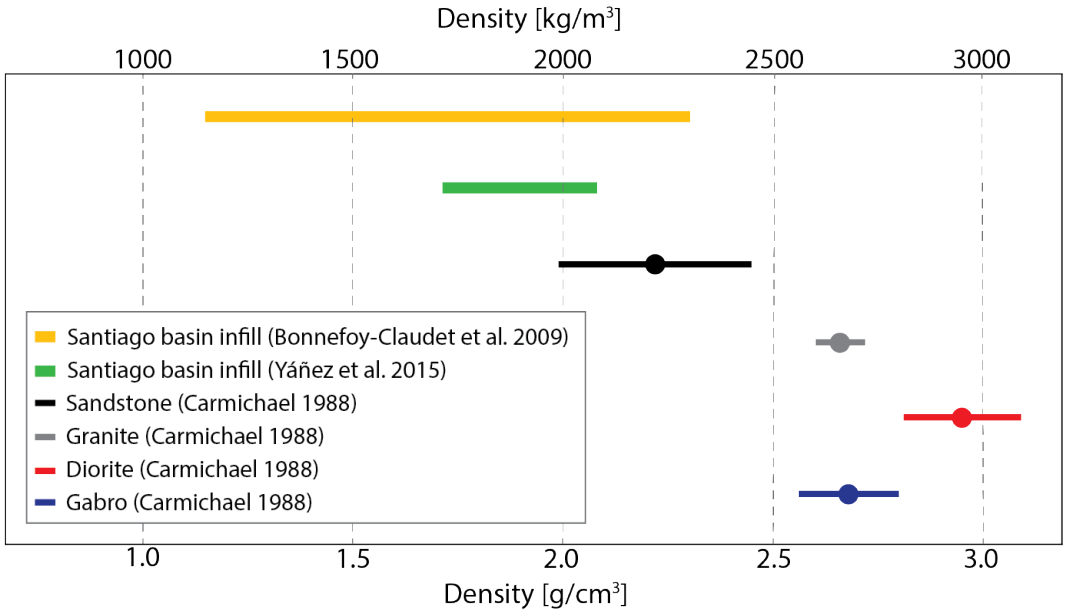

Figure 2.3: Density ranges of rocks and sediments similar as the ones observed in the study area. In the case of the sediments, only ranges were found, for the rocks, the circle correspond to the mean value and the line to the standard deviation. Obtained from Carmichael (2017), (Yáñez et al., 2015) and Bonnefoy-Claudet et al. (2009).

In many cases, the densities inferred from gravimetric measurements can be attributed to either sedimentary basements or fractures in rocks, and both are important hydrogeologic features.

2.3. Transient Electromagnetic (TEM)

2.3.1. General concepts

The transient electromagnetic (TEM) method is an active geophysical prospecting technique that uses Maxwell's equations to measure a decaying electromagnetic field, and thus estimates an apparent resistivity curve. In this thesis only a general idea of the theory that supports this method will be shown, a more thorough explanation can be found in Nabighian and Macnae (1991), Asten (1987), Montecinos (2019) and Blanco (2016).

To perform a TEM measurement, the necessary elements are a transmitter (Tx-coil), a recieving coil (Rx-coil), a computer and a power source, these elements are shown in Figure 2.4 (a). To perform the measurement, a pulse-like current that changes directions is circulated through the transmitter, as seen in Figure 2.4 (b). Due to this abrupt change in the current, currents called eddy currents are induced in the ground. Immediately after the current has turned to zero, the eddy currents are confined to the surface, and so there is no change observed in the induced magnetic field, but as the eddy currents propagate outwards and downwards, a decrease in the induced magnetic field is observed at the surface. This secondary magnetic field decay is measured in gates, that increase in length logarithmically with time (Figure 2.4 (b) down).

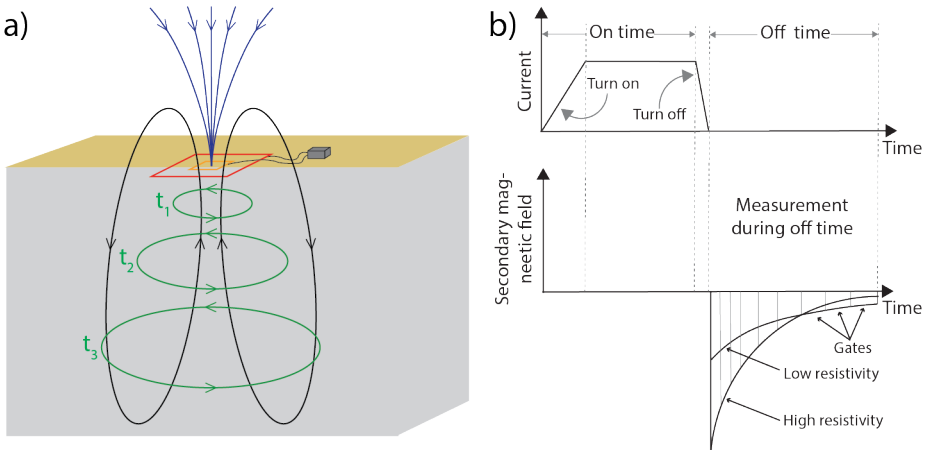

Figure 2.4: Figure a): TEM field disposition and main fields and currents asociated. The red and orange squares correspond to the Tx-coil and Rx-coil respectively. Blue arrows are the primary magnetic field, green and black ellipses are the eddy currents at times ($t_1 < t_2 < t_3$) and secondary magnetic field, respectively. Modified from Nabighian and Macnae (1991). Figure b): Up: Current shape. Down: shape of the secondary magnetic field, for a low and high resistivity ground. Modified from Asten (1987) and Christiansen et al. (2006)

The way that the diffusion of the eddy currents occurs will depend on the resistivity structure of the ground. The more conductive the structures, the slower the diffusion, and thus a slower decrease of the secondary magnetic field is observed at the surface and measured in the receiving coil (Asten, 1987).

Like all geophysical methods, TEM data has uncertainty. If the uncertainty has a random behaviour, the signal to noise ratio can be made smaller by performing a number of measurements and then stacking them. For TEM, this is the case of signals coming from electrical supply cables, lightning and electromagnetic signals from electronic devices. Nevertheless, there is another error source that, because of its deterministic behaviour, it cannot be referred to as noise. This is called coupling, and can be divided in galvanic and capacitive (Sørensen et al., 2000)

Galvanic coupling occurs when there is direct electrical contact or conductive connection between the transmitter and receiver. It normally occurs when there is a metallic conductor that allows the current to flow directly from the transmitter to the receiver, such as high voltage power lines and animal fences (Christiansen et al., 2006). Its effect can be very hard to identify on the data (Figure 2.5).

Capacitive coupling is generated when there is a metallic object buried in the ground, that produces an inductive return path to the ground (Christiansen et al., 2006). This coupling is easier to recognize, due to its oscillating nature, as seen in Figure 2.5.

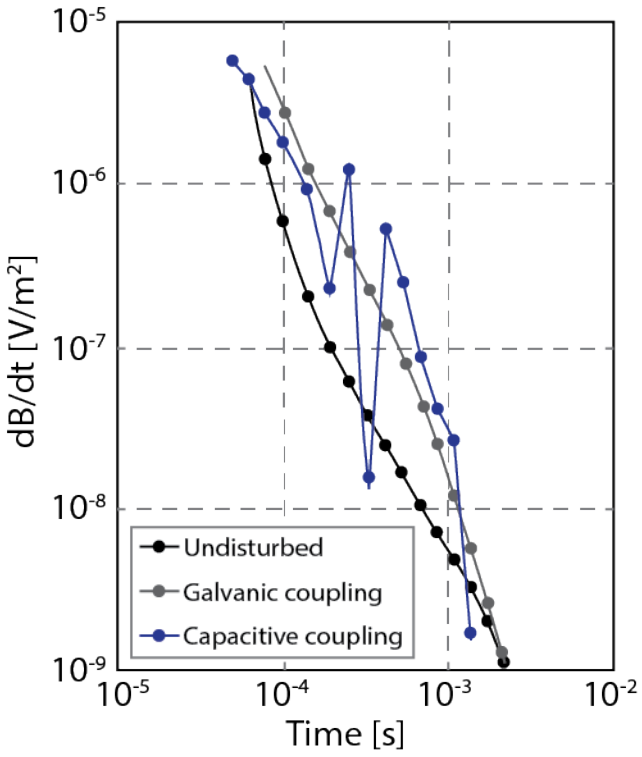

Figure 2.5: Effects of capacitive and galvanic coupling in TEM data, modified from Christiansen et al. (2006)

Through mathematical derivation, it is possible to reach an analytical expression for the vertical derivative of the induced secondary magnetic field for a constant resistivity medium, in function of other variables, assuming a circular transmitter of radius a. $\dot{b_z}(0,0,t)$ is the vertical derivative of the secondary magnetic field at the origin (defining the position of the

Rx-coil as the origin), I_0 is the amplitude of the current, σ is the electrical conductivity of the medium, $\rho = 1/\sigma$ is the electrical resistivity of the medium, a is the radius of the circular Rx-coil, μ_0 is the magnetic permeability of vacuum, erf is the error function, and $x = 1/4\tau$, $\tau = t/t_c$ and $t_c = \mu_0 \sigma a^2$.

$$\dot{b_z}(0,0,t) = -\frac{I_0 \rho}{\mu_0 a^3}\left[3\mathrm{erf}(x) - \frac{2}{\sqrt{\pi}} x(3+2x^2)e^{-x^2}\right] \tag{2.5}$$

To obtain the apparent resistivity, is useful to consider two scenarios (a) early times ($t \longrightarrow 0$), and (b) late times ($t \longrightarrow \infty$). For each of these cases, the apparent resistivity can be approximated as shown in equations 2.6 and 2.7. The Figure 2.6 shows the both approximations for the case of a 10 [Ωm] constant resistivity ground.

$$\rho_{a,et} = -\frac{3I_0}{\sigma a^3}\dot{b}_{z,et} \tag{2.6}$$

$$\rho_{a,lt} = -\left[\frac{I_0 a^2}{20\sqrt{\pi}}\right]^{2/3} t^{-5/3} \mu_{5/2} \dot{b}_{z,lt}^{-2/3} \tag{2.7}$$

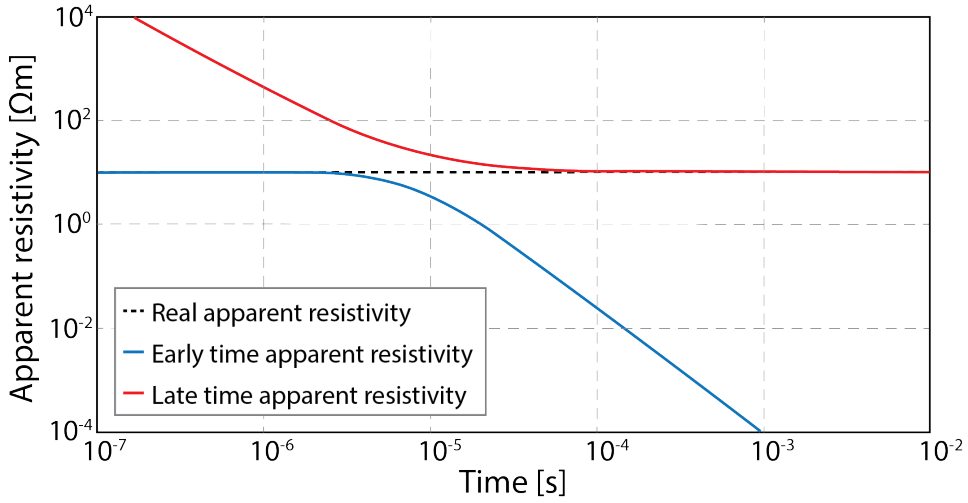

Figure 2.6: Early time and late time apparent resistivity approximation for a 10 [Ωm] resistivity ground. Modified from Montecinos (2019).

2.3.2. Data acquisition

To acquire the transient electromagnetic data, the equipment used was the ABEM WalkTEM, property of the Geophysics Department of *Universidad de Chile*. This equipment is composed of four parts: the transmitter cable, the receiving antennas, the console and the power source.

The transmitter is the component that conducts the current. This current has a step-function waveform (Figure 2.4 (b)). The transmitter cables used in this work, were squared 20 x 20 m^2 and 40 x 40 m^2 cables. It is necessary to connect a damping resistance in parallel to the transmitter loop, and so a 200 Ω resistance was used. The receiving antennas

used were the two included with the ABEM WalkTEM. The first one, called RC-05, is a squared 0.5 x 0.5 m^2, in which the internal cable gives 20 turns inside the antenna, giving it an effective induction area of 5 m^2 (hence the name). The second antenna is called RC-200, a squared antenna of 10 x 10 m^2, with two turns inside, and 200 m^2 of effective induction area.

The console is the computer that contains the programs and ports necessaries to perform the measurements. It allows to select the experimental configuration and the script used to acquire the data. The script used was one predefined in the equipment, called `DualMoment_30_40`, that performs 40-gate sweeps, adding up to a total time of 30 ms. For each cycle, 28 sweeps are measured: 13 sweeps are performed at a 225.5 [Hz] frequency and a current of 1 [A] (low moment), 13 sweeps with a 7 [A] current (high moment) at a 12.5 [Hz] frequency, and two sweeps with no current, in order to measure the background noise. A central loop array was used, using both RC-05 and RC-200 antennas. The power source was a 12 [V] car battery.

Of the 8 stations that were acquired, one clearly showed inconsistencies in the data (Figure 2.7 (c)) and thus wasn't modelled. The station TEM 9 was measured underneath a medium voltage tower, and wasn't modelled due to possible galvanic coupling. The figure 2.7 shows the location of all TEM stations, and the example of the acquired data of two of them: TEM 17 and TEM 20. In this case, the station TEM 20 was modelled, while the station TEM 17 was not.

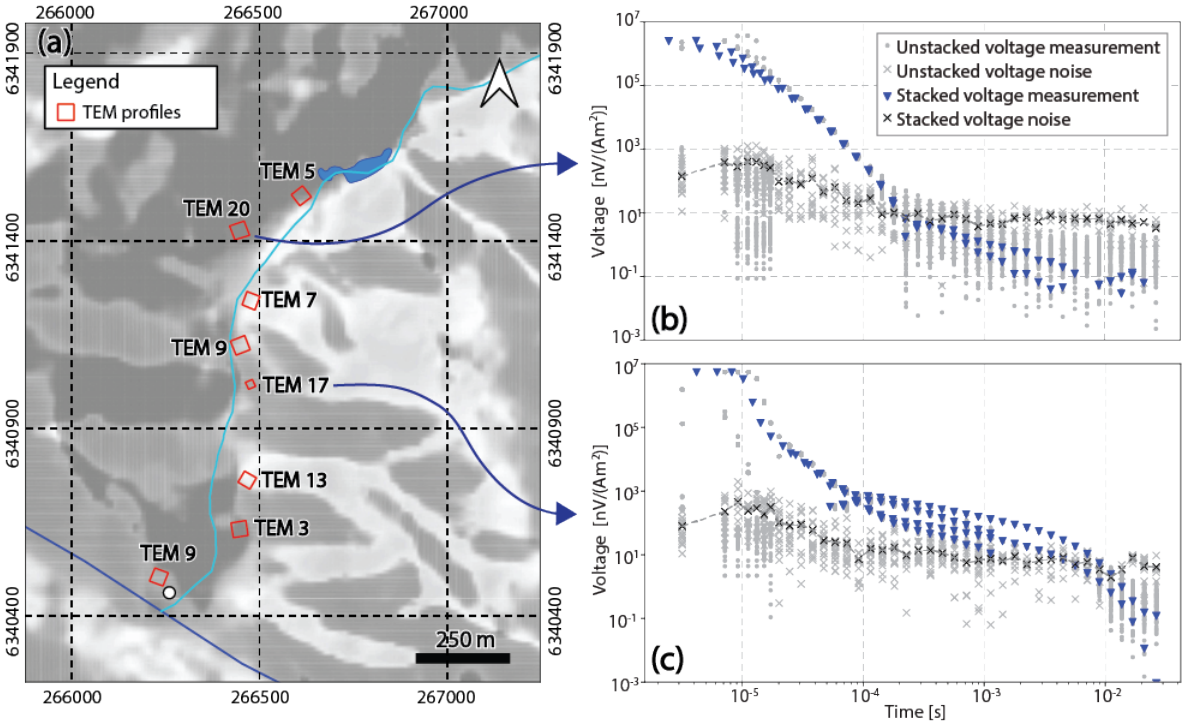

Figure 2.7: Figure (a) locations of all measured TEM stations, also showing the artifitial lagoon (blue polygon), the Linneo stream (light blue line), the Marga-Marga stream (blue line), and the pumping well (white dot). Figure (b): Data acquired for the station TEM 20, wich shows good data quality and was inverted. Figure (c): Data acquired for station TEM17, wich shows a significant difference in the voltage measured for different antennas in times later than 10^{-4} [s].

Given that the data was measured using two antennas with different effective area, and that smaller antennas are better to measure early times, the following criterion was defined, with the purpose of modeling only the data points that had more validity:

- For times inferior to 10^{-4} s, the data points obtained with the RC-05 antenna were used.
- For times between 10^{-4} y $2 \cdot 10^{-4}$ s, the data points obtained with the RC-200 antenna were used.
- For times superior to $2 \cdot 10^{-4}$ s, the data points were not used.

The filtering process was done with the same program later used for the inversion, called Interpex 1D. This program allows to convert the voltage to apparent resistivity. An example of the filtering process and conversion to apparent resistivity is shown in Figure 2.8.

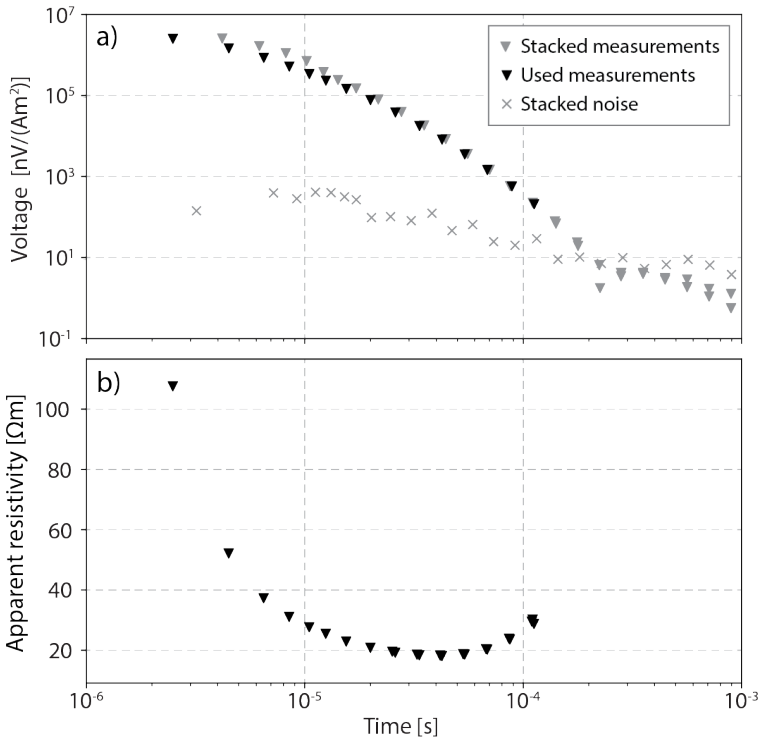

Figure 2.8: Up: Data of station TEM20, showing all points measured (gray triangles), the level of noise (gray crosses), and the data point used to model (black triangles). Down: Apparent resistivity asocciated with each of the voltage measurements used to model the data

2.3.3. Inversion of TEM data

Once filtered, three inversions were performed for each station, a 15-layer model using the Levenberg-Marquardt algorithm, a 15-layer model using the Occam algorithm, and a 3-layer model using the Levenberg-Marquardt algorithm. A three layer model was used for interpretation because, given the lack of geological constraints, an assumption was made to make the models with as few layers as possible, and in this case that meant three layers, because two-layered models did not properly fit the data. The program used to perform the inversions allows to obtain a series of equivalent models, that is, a group of three layer models that have a RMS value of up to 1.2 times the RMS of the best fit model. It is important to mention that the three layer model chosen was always the one with the smallest RMS.

2.3.3.1. The Levenberg-Marquardt algorithm

The Levenberg-Marquardt algorithm is an iterative method that, starting from a model k, updates such model according to the equation:

$$m^{k+1} = m^k + \Delta m^k \tag{2.8}$$

Where Δm^k is obtained from:

$$\left[J_F^T(m^k) + \lambda \cdot I\right] \cdot \Delta m = -J_F^T(m^k) \cdot F(m^k) \tag{2.9}$$

From equation 2.9, $F = [f_1(m^k), f_2(m^k), \ \ldots \ , f_N(m^k)]^T$ is the function that is minimized, J_F is the jacobian matrix of F, I is the identity matrix and λ is a constant that controls the amplitude of Δm^k (Marquardt, 1963; Madsen et al., 2004).

2.3.3.2. The Occam Algorithm

The Occam algorithm is a version of a regularized least-square optimization (Constable et al., 1987), of the form:

$$\min_m E(m) + \varepsilon^2 L(m) \tag{2.10}$$

Where $E(m)$ is the forward function, $L(m)$ is a function of m, some examples are the norm, the gradient or the laplacian. ε controls the weight of $L(m)$ in the minimization.

The Figure 2.9 shows all different models for station 20, including all equivalent models. All models were inverted with an initial resistivity of 100 [Ωm]. Models with 4 layers or more were also inverted, but showed only a marginal improvement of the RMS value. The model showed in black line is the one later used for interpretations.

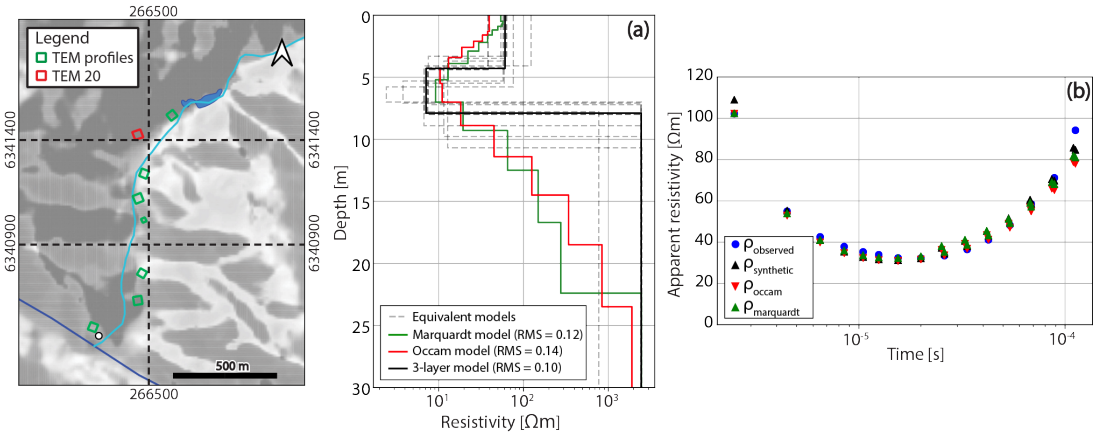

Figure 2.9: (a): Inversion results for station 20, including the best fit 3-layer model, its equivalent models, and the 15-layer occam and marquardt models. (b): observed apparent resistivity (blue) and the predicted data for the 3-layer model (black), the smooth occam model (red) and the smooth marquardt model (green).

2.4. Electrical Resistivity Tomography (ERT)

2.4.1. General concepts

ERT is a an active geophysical method, that estimates the apparent resistivity of the ground, through injecting a current and measuring the associated electrical potential difference (voltage). A schematic example is depicted in Figure 2.10.

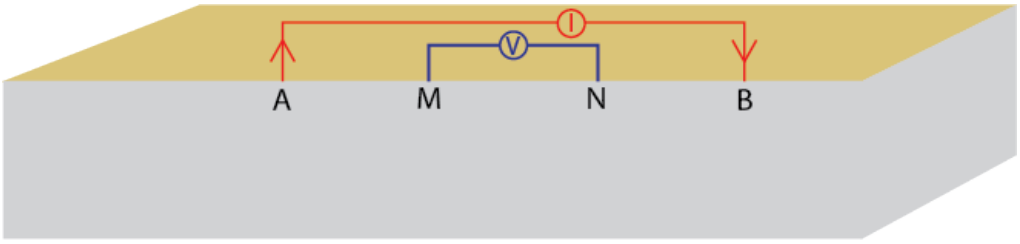

Figure 2.10: ERT array, the current is injected in electrodes A and B, and voltage is measured in electrodes M and N.

From the calculus and subtraction of the potentials of electrodes M and N, the difference of potential can be written as shown in equation 2.11 (Samouëlian et al., 2005), and so the apparent resistivity can be calculated as seen in equation 2.12

$$\Delta V = U_M - U_N = \frac{\rho I}{2\pi}\left[\frac{1}{AM} - \frac{1}{BM} - \frac{1}{AN} + \frac{1}{BN}\right] \tag{2.11}$$

$$\rho = \frac{\Delta V}{I}\frac{2\pi}{\left[\frac{1}{AM} - \frac{1}{BM} - \frac{1}{AN} + \frac{1}{BN}\right]} \Longrightarrow \rho = \frac{\Delta V}{I}\cdot k \tag{2.12}$$

From equation 2.12 is evident that the apparent resistivity is equal to the voltage divided by the current (a resistance) multiplied by a factor k. This is called geometric factor, because it corrects the dependence of the electrode locations in the measurement. The resistance has units of [Ω], and so the resistivity ρ has units of [Ωm]. The scheme of Figure 2.10 actually returns a single value of resistivity, that by convention is associated to a depth of $AB/2$, and located right in the middle of electrodes M and N. To obtain a 2D resistivity pseudosection, it is necesary to successively change the location of the electrodes. The figure 2.11 shows how, changing the electrode separation and location, it is possible to generate a complete 2D profile of apparent resistivity.

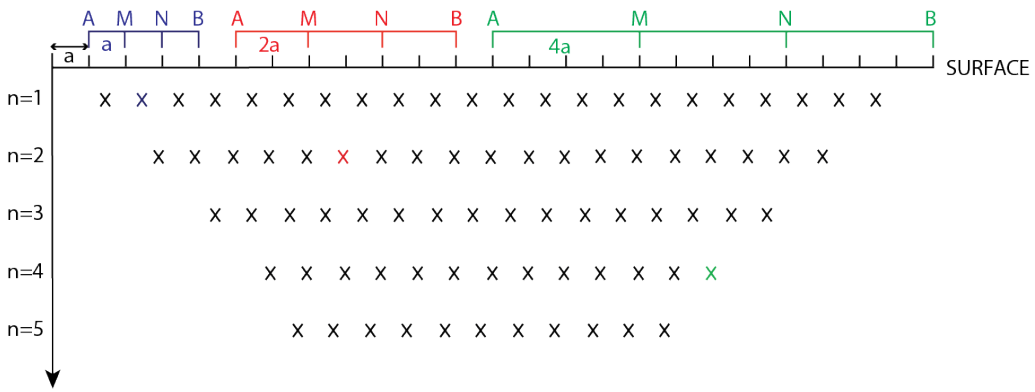

Figure 2.11: 2D electrical resistivity pseudosection using a Wenner-Schlumberger array. A and B correspond to current electrodes, and M and N correspond to voltage electrodes. Each cross marks an observation made with a specific combination of electrodes, the different depths correspond to observations made with a distinct electrode separation. Modified from Samouëlian et al. (2005)

2.4.2. Data acquisition

The ERT data was a acquired using an IRIS pro Switch II, property of the department of Geophysics of *Universidad de Chile*. Besides the console, two 24-channel cables and 48 metalic electrodes were used. The power source was a 12 [V] car battery. The array chosen was dipole-dipole. The longitud of the profiles varied from 24 to 240 meters. The goal was always to achieve the longest profile possible, but because the study area was a public park, it was often necessary to avoid certain zones due to people or vehicles. A similar comment can be made about the orientation of the profiles, it was attempted to orient them either parallel or perpendicular to the watershed flow direction, but that was limited also by in situ considerations (eg. buildings, vehicles or animals).

The locations and orientation of the profiles can be seen in Figure 2.12, as well as the data of two ERT profiles. Profile ERT 10 is located next to the pumping well and profile ERT 11 is located parallel to the Olivar stream. From the eight ERT profiles, three of them (ERT 5, ERT 6, and ERT 9) were discarded because of their poor quality data, identified as extremely high or even negative resistivities.

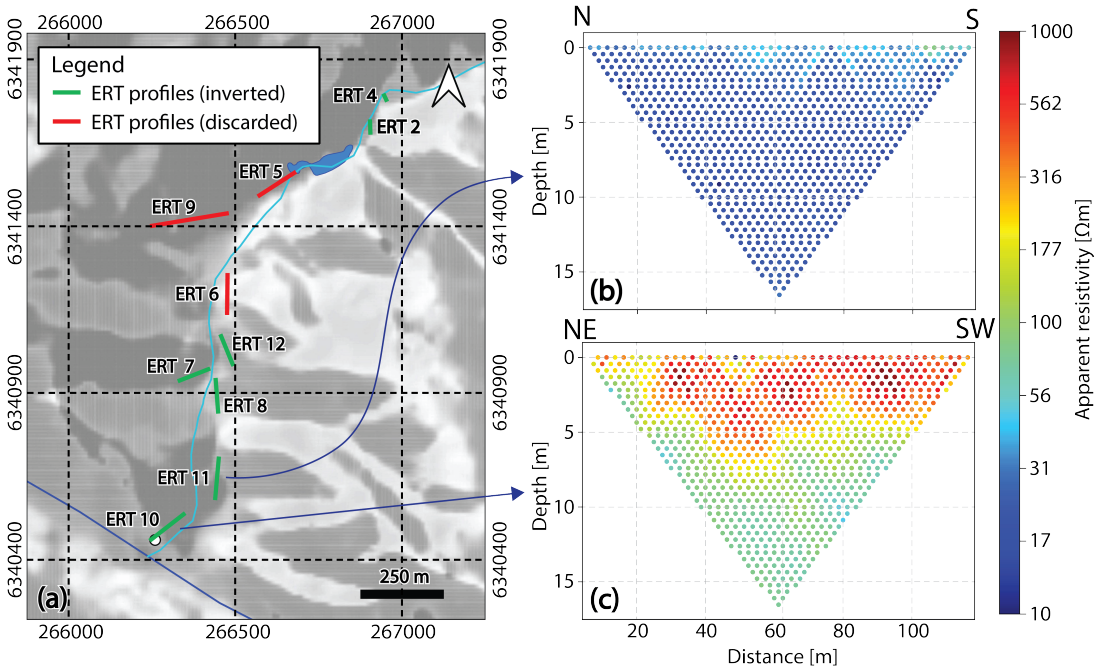

Figure 2.12: Figure (a): Map showing the locations of all ERT measurements. Figure (b): apparent resistivity obtained for profile ERT 11. Figure (c): apparent resistivity obtained for profile ERT 10, right next to the well

2.4.3. Inversion of ERT data

The ERT inversion was performed using the commercial program DCIP2D, that uses a least-squares algorithm. A complete documentation can be found in the promgram's web page (https://dcip2d.readthedocs.io/en/latest/). Here, only a description of the inversion algorithm will be made. The global misfit criterion is shown in Equation 2.13, where G is the

function that receives a model m as input and returns the predicted data (forward model), d is the measured data, and W_d is a weight matrix defined as $W_d = diag\{1/\varepsilon_1, ..., 1/\varepsilon_n\}$, being ε_i the standard deviation of the i-th data point.

$$\psi_d = \|W_d(G \cdot m - d)\|^2 \tag{2.13}$$

In the Equation 2.14, the continuous form of the objective function is shown. This function, minimizes both the vertical and horizontal variations of the model, as well as the difference with the initial model m_0.

$$\begin{aligned}\psi_m(m, m_0) = \alpha_s \int\int w_s(x,z)(m-m_0)^2 dxdz \\ + \int\int \left[\alpha_x w_x(x,z)\left(\frac{\partial(m-m_0)}{\partial x}\right)^2 + \alpha_z w_z(x,z)\left(\frac{\partial(m-m_0)}{\partial z}\right)^2\right] dxdz\end{aligned} \tag{2.14}$$

In Equation 2.14, α_s, α_x and α_z are constants that control the weight of the closeness with the initial model, the horizontal and vertical smoothness of the resulting model, respectively. The result in Equation 2.15 is the discrete form of the objective function.

$$\begin{aligned}\psi_m(\vec{m}, \vec{m_0}) &= (\vec{m} - \vec{m_0})\left[\alpha_s W_s^T W_s + \alpha_x W_x^T + \alpha_z W_z^T W_z\right](\vec{m} - \vec{m_0})^T \\ &= (\vec{m} - \vec{m_0})^T W_m^T W_m (\vec{m} - \vec{m_0})^T \\ \psi_m &= \|W_m(\vec{m} - \vec{m_0})\|^2\end{aligned} \tag{2.15}$$

Finally, the complete inversion algorithm can be formulated as follows:

$$\begin{aligned}\min_m \quad & \psi_m(\vec{m} - \vec{m_0}) = \|W_m(\vec{m} - \vec{m_0})\|^2 \\ \text{s.t.} \quad & \psi_d(\vec{d}, \vec{d^{obs}}) = \|W_d(\vec{d} - \vec{d^{obs}})\|^2 = \psi_d^*\end{aligned} \tag{2.16}$$

In words, the algorithm finds the model that is closest to the initial model, that minimizes vertical and horizontal variation and that has a value of ψ_d equal or smaller than ψ_d*. The initial model for each profile was the best fitting constant resistivity. As an exercise, a series of different combinations of the user defined parameters were tested in one particular profile, to evaluate the difference in the resulting resistivity models (Figure 2.13). The profile chosen was ERT 10, and the parameters varied were α_s, α_x and α_z.

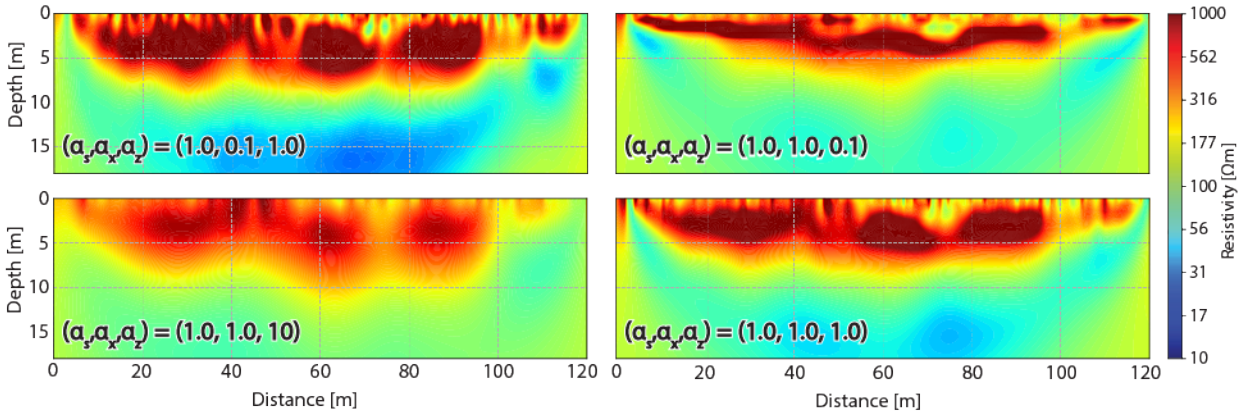

Figure 2.13: Different inversions for profile ERT 10, varying the parameters α_x and α_z

The parameters chosen for the final inversion were $(\alpha_s, \alpha_x, \alpha_z) = (0.7, 1.0, 1.0)$. α_x and α_z were chosen as 1.0, because there is no a priori information to assume a particular roughness or smoothness in either x or z direction, α_s was chosen as 0.7, because it was considered a good trade-off between smoothness and data misfit. All the profiles were inverted with a constant resistivity value (shown in Table 2.1) as initial model.

Table 2.1: Resistivity and depth range for all the three layered models.

Profile	**Initial resistivity [Ωm]**
ERT 2	162
ERT 4	146
ERT 7	54
ERT 8	47
ERT 10	141
ERT 11	25
ERT 12	24

Figure 2.14 shows the comparison between the acquired data and the inverted model for station ERT 10. As seen in Figure 2.13, the inverted resistivity model has a rectangular shape. The information of the lower left and lower right part of the model were not shown, as there is no acquired data points in those areas.

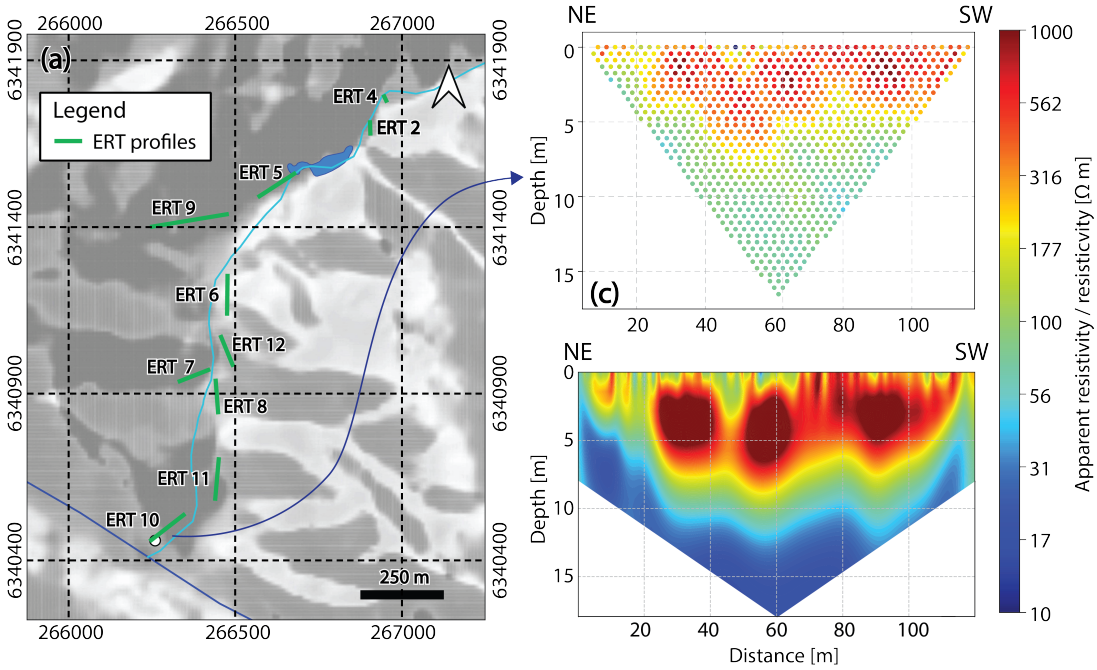

Figure 2.14: (a): Acquired data for profile ERT 10. (b) Inverted model for profile ERT 10

2.5. Gravimetry

2.5.1. General concepts

The gravimetry is a geophysical prospecting tenchnique that is based on the measurement of the gravimetric signature of density variations of the subsurface (Hinze et al., 2013). Mainly due to topography and density variations in the ground, the Earth's gravity field has variations. In order to calculate an anomaly, it is necessary to define a theoretical equipotential surface, known as the reference ellipsoid. This surface is generated by rotating an ellipse over its smaller axis, and its mathematical expression is shown in equation 2.17. The real Earth's equipotential surface is called geoid, and the difference between the geoid and ellipsoid is called geoid ondulation (N in Figure 2.15).

$$g_0 = g_e \left(\frac{1 + k\sin^2\lambda}{\sqrt{1 - e^2\sin^2\lambda}} \right) \tag{2.17}$$

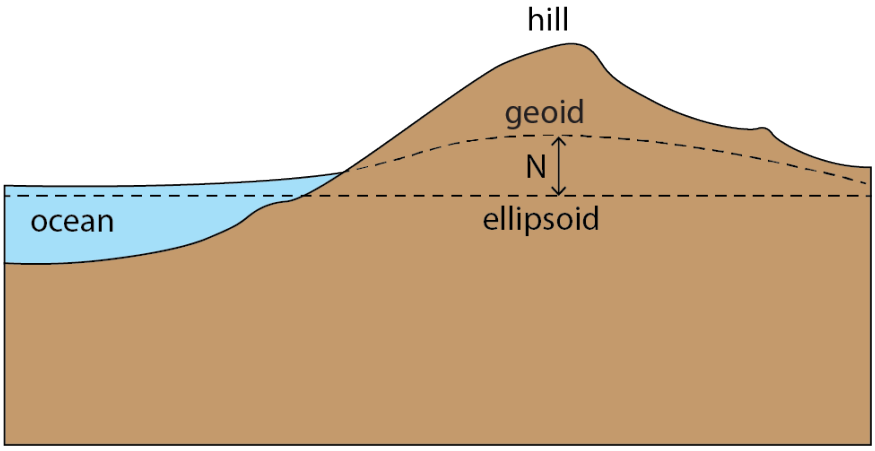

Figure 2.15: Schematic representation of geoid and ellipsoid surfaces, modified from Lowrie and Fichtner (2020).

Once corrected, the difference between the theoretical gravity and measured gravity, called gravimetric anomaly, can be solely attributed to subsurface density variations. The corrections performed in this work were (1) earth tide correction, (2) instrumental drift correction, (3) Bouguer correction, (4) free air correction, (5) topographic correction and (6) regional correction. Detailed explanaiton of each of these corrections can be found in Lowrie and Fichtner (2020), Hinze et al. (2013), and (Martín, 2023).

2.5.2. Won-Bevis algorithm

The forward modelling was made using the Won-Bevis algorithm (Won & Bevis, 1987), to compute the gravimetric anomaly produced by a polygon. This algorithm was implemented using Python. According to the authors, the vertical component of the gravimetric anomaly can be calculated as shown in equation 2.18 and Figure 2.16. The program, written specifically for this thesis, made it possible to consider any number of polygons, with different shapes, positions and density contrasts.

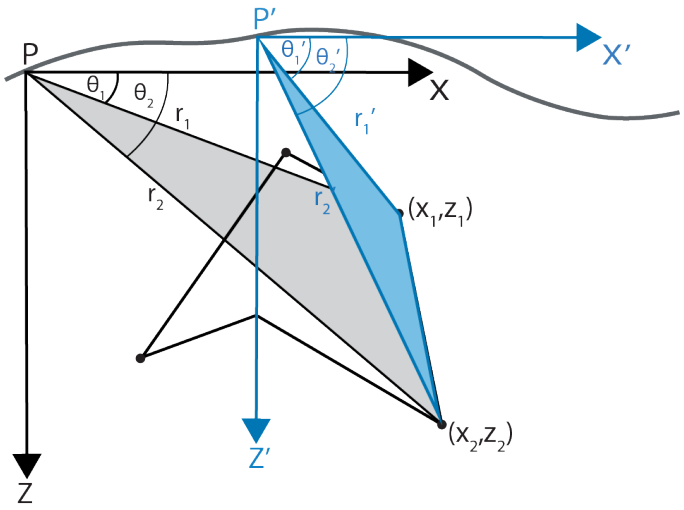

Figure 2.16: Scheme of the elements used to calculate the gravity anomaly, showing the displacement of the location from where the anomaly is calculated. Modified from Won and Bevis (1987). The topographic surface is represented by the gray line.

$$\Delta g_z = 2\rho G \sum_{n=1}^{N} \frac{\beta_n}{1+\alpha_n^2}\left[\ln\frac{r_{n+1}}{r_n} - \alpha_n(\theta_n+1) - \theta_n\right] \tag{2.18}$$

From equation 2.16, the different elements are defined as follows:

$$\alpha_n = \frac{x_{n+1}-x_n}{z_{n+1}-z_n},\ \beta_n = x_n - \alpha_n z_n = x_{n+1} - \alpha_{n+1} z_{n+1} \tag{2.19}$$

$$r_n = \sqrt{x_n^2+z_n^2},\ r_{n+1} = \sqrt{x_{n+1}^2+z_{n+1}^2} \tag{2.20}$$

$$\theta_n = \arctan\frac{z_n}{x_n},\ \theta_{n+1} = \arctan\frac{z_{n+1}}{x_{n+1}} \tag{2.21}$$

2.5.3. Acquisition

For the gravimetric survey, a Scintrex CG3 gravimeter was used, and the position was measured using a TOPCON HIPER-V differential GPS. A total of 60 points were measured, their locations and example gps data of one station are shown in the Figure 2.17. Each measurement consisted in a 30 second gravity time series, and an aproximately 5 minute time series for the GPS (Figure 2.17 (b))

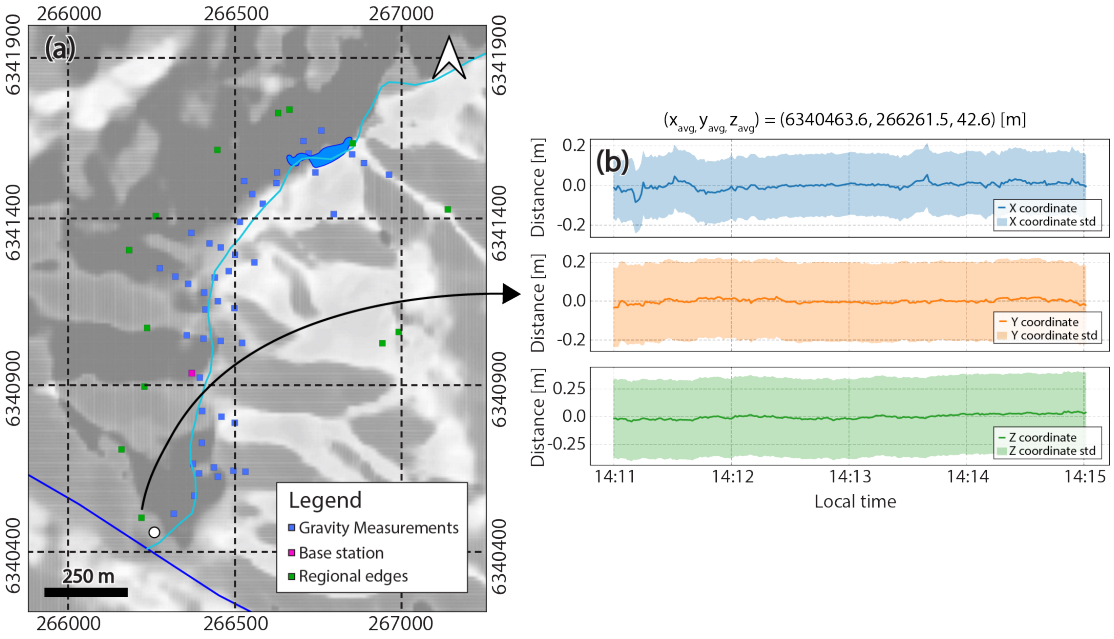

Figure 2.17: Figure (a): Location of all gravimetric stations and gps data of one station. Figure (b): GPS time series of a station, showing the deviation of the calculated average position for each coordinate, seen in the title. The std of the time series is shown in a light color.

2.5.4. GPS data processing

Given that the gravimetric data reduction process includes two elements that consider the distance from the observation point to the georreference datum, it is very important to have a precise vertical location of where the gravimetric data was obtained. The GPS data was processed using the precise point positioning technique (PPP). This technique processes the data of a single GNSS reciever, using satellite constellation orbits and clock offsets, determined separately (Bisnath & Collins, 2012). The goverment of Canada offers a free service online to perform this processing (https://webapp.csrs-scrs.nrcan-rncan.gc.ca/geod/tools-outils/ppp.php, Mireault et al. (2008)). Recieving the data of each station, this web page returns a time series with the standard deviation for each coordinate (x, y and z), as it is shown in Figure 2.17. These time series were then processed to obtain an average value and an average standard deviation, for x, y and z coordinates.

2.5.5. Data reduction

Once the data was measured, a reduction process was performed following the normal steps of earth tide correction (ETC), instrumental drift, Bouguer correction, free air correction, topographic correction and regional tendency correction.

The ETC was done using a MATLAB script that calculates one correction value for each minute, given a date and a location, according to the algorithm proposed by Longman (1959). The instrumental drift correction was performed measuring at least at the beginning and end of the day the gravity in a base station, and then extracting the linear trend associated to this measurements. This linear trend of one day of the field campaign is shown in Figure

2.18. The topographic correction was done in the Oasis Montaj program, using the SRTM 30 x 30 m^2 pixel digital elevation model (DEM) as input.

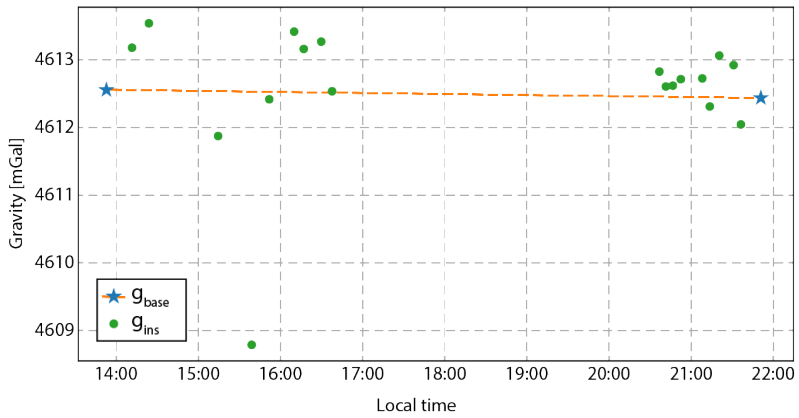

Figure 2.18: Gravity measurements performed during may 18th (green dots), also showing the base measurements (blue stars) and the interpolated instrumental drift (dashed orange line)

The correction by regional tendency was made following a series of steps. First, the data points on the edge of the anomaly were selected (green squares in Figure 2.17). Second, the plain with the smallest difference with the selected data points was calculated, and then subtracted from all the measurements. Once the result for each data was obtained, the anomaly was interpolated to obtain a continuous anomaly in the study area. The Figure 2.19 shows the regional tendency obtained, and the data once corrected by this tendency.

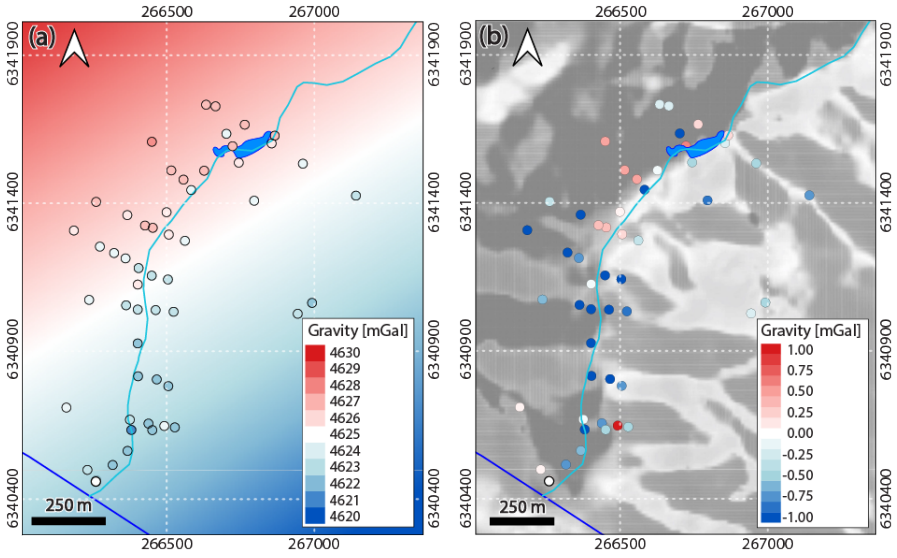

Figure 2.19: Figure (a): Complete Bouguer anomaly (color dots) over the obtained regional anomaly. Figure (b): Anomaly without the regional tendency.

2.5.6. Forward modelling

Once the gravimetric data reduction (Won & Bevis, 1987), explained in the section 2.5.1. To reproduce the gravimetric anomalies, three bodies were used, that are summarized in Table 2.2. The types of bodies were chosen according to the available geological information, and the Sedimentary Unit *Potrero Alto* was not considered in an attempt to not over complicate the model. Next, a description of why these densities were chosen is given:

- **Sediments**: A value was chosen within the density range shown in Figure 2.3. As the *Potrero Alto* unit was not modelled, and it is likely that this unit has a higher degree of compaction, it was consider appropriate that the chosen value was in the higher end of the density range, thus a value of 2000 [kg/m^3] was selected.
- **Intrusive**: The value elected was very close to the average density value of diorite according to Carmichael (2017) (2950 kg/m^3).
- **Fractured basement**: The density contrast assumed between normal and fractured basement is consistent with the one used by Martín (2023) and Marti et al. (2023). If we use the porosity equation $\phi = (\rho_m - \rho)/(\rho_m - \rho_p)$, where ϕ is the porosity, ρ is the density of the fractured basement, ρ_m is the background density and ρ_p is the density of the pores, we can calculate that for the density 2370 [kg/m^3], the porosity of the basement would be 11.2% for air filled fractures, and 17.9% for water filled fractures.

Table 2.2: Densities and density contrasts of the bodies used to model the gravimetric anomalies of the profiles. The background density to calculate the density contrasts was 2670 [kg/m^3]

Body	Density (ρ)	Density contrast ($\Delta\rho$)
Sediments	2000 [kg/m^3]	-670 [kg/m^3]
Intrusive	2970 [kg/m^3]	300 [kg/m^3]
Fractured basement	2370 [kg/m^3]	-300 [kg/m^3]

2.6. Hydraulic conductivity

An aquifer can be defined as a geologic unit that can store and transmit water (Fetter, 2018). Some units that can be aquifers include sands, gravels, sandstones and fractured plutonic and metamorphic rocks. In the aquifers, empty (air filled) spaces become saturated with water. This space is called porosity, and can be classified in primary and secondary. The primary porosity is associated to void spaces formed at the same time that the unit, this is the case of the porosity of sedimentary units. The secondary porosity, on the other hand, is formed after the unit, this is the case of porosity due to fractures in plutonic of metamorphic rocks.

Hydraulic conductivity is an important property of the aquifers, and can be defined as its ability to transmit water (Fetter, 2018). It was first sistematically studied by Henry Darcy in the 1800s (Darcy, 1856). He proposed the so called Darcy's law (Equation 2.22).

$$q = -K\frac{dh}{dl} \tag{2.22}$$

where $q = Q/A$ is the specific discharge. Q is the discharge, measured in volume $\cdot$ time^{-1}, and A is the area throw where this discharge flows. Specific discharge has then, units of length $\cdot$ time^{-1}. dh/dl is called hydraulic gradient, and is the difference in head (water level) between to points, divided by their distance, it is an adimensional parameter. Thus, K is the parameter that linearly relates these two quantities, and has the same units that q. This parameter K referred to as the hydraulic conductivity.

The hydraulic conductivity depends upon parameters such as the porosity and fracture density, and determines, among other things, the infiltration rate of the water from the surface to the aquifer. In a very general classification, some values of hydraulic conductivity are shown in Table 2.3 (Bouwer et al., 1999).

Table 2.3: Hydraulic conductivity of different soil types (Bouwer et al., 1999)

Soil type	**Hydraulic conductivity [m/day]**
Clay soils	< 0.1
Silts	0.2
Sandy silts	0.3
Silty sands	0.5
Fine sands	1
Medium sands	5
Coarse sands	> 10

Regarding the connection between geophysical resistivity observations and hydraulic conductivity, the main idea is that the electrical properties are related to the petrophysical parameters that control fluid transport on the ground. Thus, the estimation of hydraulic conductivity from resistivity is possible (as seen in Chen et al. (2001) and Niwas et al. (2011)), but a proper estimation requires either a frequency dependent resistivity measurements, or other types of constraints such as seismic data or sparse hydraulic conductivity measurements (Slater, 2007).

Chapter 3

Study area

3.1. Geological Setting

As mentioned before, the only available geological information concerning the study area is the Valparaíso-Curacaví geological map (de Geología y Minería et al., 1996). In this map, five units are recognized, which are the Laguna Verde unit (Jlv), Lliu Lliu unit (Jlg), Potrero Alto stratums (TQpa), Sauce unit (Js) and an intrusive paleozoic unit (Pzmg). These can be seen in the Figure 3.1.

The intrusive units correspond to the Laguna Verde, Lliu-Lliu, Sauce and the paleozoic Units. The Laguna Verde Unit (the pale pink unit with dots, present in the south east of the study area) is composed of amphibolite, diorites, monzodiorites and gabbros. It contains between a 45 and 60% of silica, and its age ranges between 155 and 157 Ma. The Lliu LLiu unit (pale brouwn unit visible between 6340500 and 6341000 Y UTM coordinates, and around 266000 X UTM coordinate in Figure 3.1) is formed by amphibole-biotite monzogranites. Its silica content is 70 - 75%. There are no reported ages for this unit. The Sauce unit is predominantly composed of quartz diorites tonalites and subordinated gabbros, the silica percentage is 45-60%, and reported ages are 155 to 157 Ma. Lastly, the Pzmg (red unit towards the west on Figure 3.1) is a paleozoic unit formed by tonalites, granodiorites, monzogranites and granites. Its silica percentage varies betwenn 65 and 80 %. Measured ages cover the range between 290 and 405 Ma, depending on the mineral.

The Potrero Alto Stratums (pale dark yellow in the center Figure 3.1) are sedimentary deposits of medium to low consolidation of conglomerate, sandstones and siltstones, that are covered by a layer of quaternary alluvial deposits. The thickness of this deposit varies greatly, with a maximum value of 50 m, according to de Geología y Minería et al. (1996).

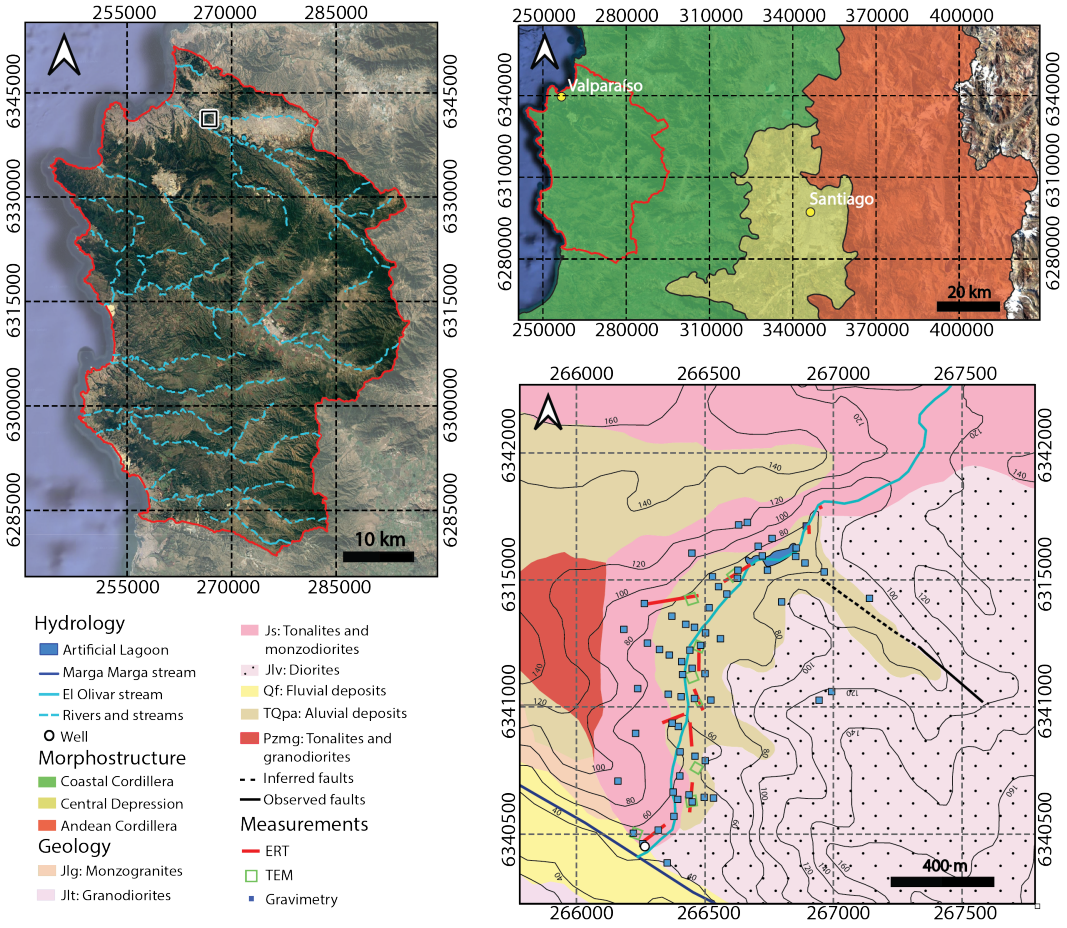

Figure 3.1: Location, geology, hydrology and measurements taken in the study area. The black and white square in the upper left map, corresponds to the location of the study area, amplified in the lower right map.

3.2. Hydrology and hydrogeology

The Viña del Mar Botanical Garden (BGVM) is placed inside a 7.5 km^2 watershed, with a north-south orientation, and is located between the cities of *Viña del Mar* and *Quilpué*, *Valparaíso Region*. Through this watershed flows a stream called El Olivar, that discharges into the Marga Marga stream, an important stream of this region. There are several elements that make this watershed of particular interest: it has a relatively small and controlable size to perform experiments, it posseses a perennial stream, it has the infrastructure for the charge and discharge of an artificial lagoon inside the BGVM, and there are records of contamination episodes due to wastewater coming form an ESVAL water treatment plant located upstream.

The climate in the area is semi arid, with most of the precipitation occuring during winter. The data obtained from the closest meteorological station has a yearly average precipitation of 482 [mm] for the period 1971-2009 (before the megadrought began) and of 210 [mm] for the period 2010-2023 (Figure 3.2). The data of 2023 was considered until July 25th.

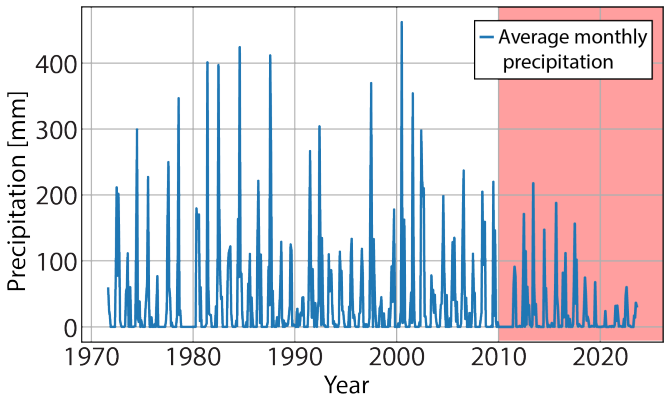

Figure 3.2: Average monthly precipitation of Roderillos meteorological station. obtained from the CR2 climate explorer (https://explorador.cr2.cl/). The red area shows the mega drought period.

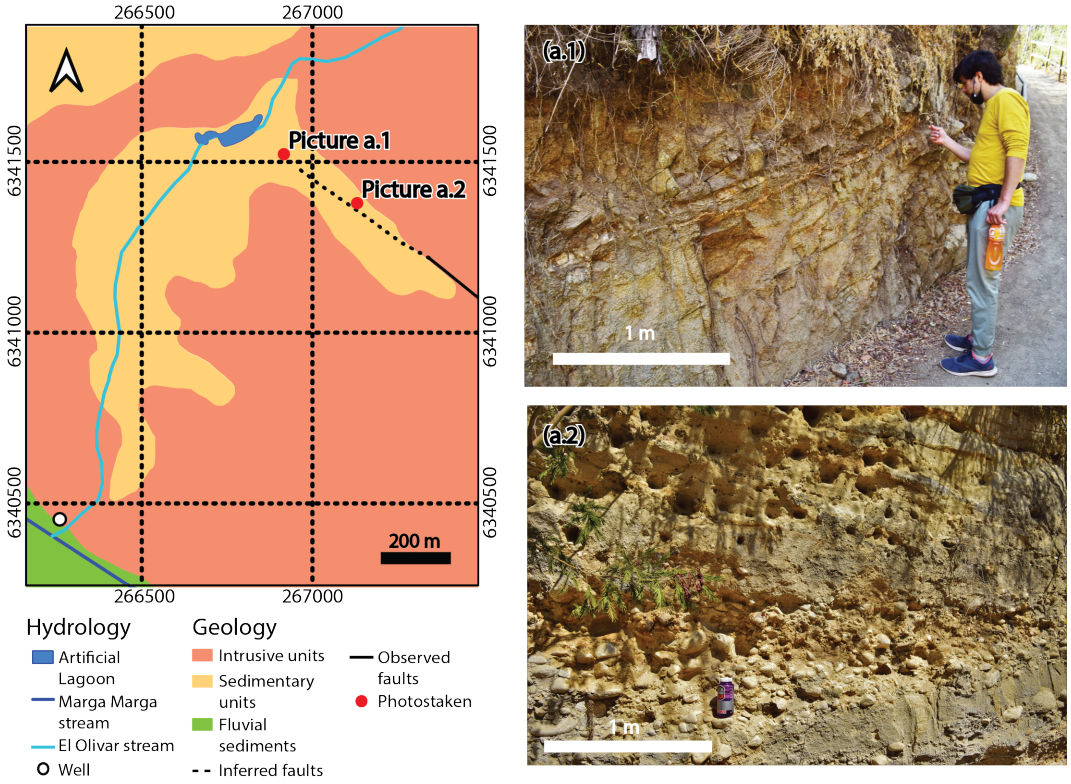

Figure 3.3: Map showing the three hydrogeologic units observed in the geological map. The intrusive units, shown in orange, correspond to the units Jlg, Jlv(a.1): picture of the sedimentary unit. (a.2): picture of weathered and fractured basement.

From a hydrogeological perspective, three main units can be defined. The first is the alluvial quaternary sediment covering the BGVM. This unit is expected to be over the Potrero Alto unit. The second unit are the sedimentary stratums Potrero Alto, and the third are the intrusives (Figure 3.3). According to Domenico and Schwartz (1998), the hydraulic conductivity of intrusive rocks ranges between $3 \cdot 10^{-14}$ m/s and $2 \cdot 10^{-10}$ m/s and so can be considered as impermeable. It is not straight forward to calculate the Potrero Alto unit

hydraulic conductivity, because its composition is not thoroughly known, and the hydraulic conductivity of sediments with different grain sizes vary greatly ($3 \cdot 10^{-4} - 3 \cdot 10^{-2}$ m/s for gravel, and $1 \cdot 10^{-11} - 4.7 \cdot 10^{-9}$ m/s for clay (Domenico & Schwartz, 1998)).

Chapter 4

Results

4.1. Transient Electromagnetic (TEM)

The TEM results are three-layer and 15-layer resistivity curves. The three-layer curves are used for interpretation, while the 15-layer curves are used as validation. Figures 4.1 and 4.2 show the models and the apparent resistivity curves of station TEM 3 and TEM 20, respectively. The resistivity structure observed in these two stations is similar, and is present in all other stations. It can be described as follows: a first layer with variable resistivity, reaching up to 6 meters deep, a conductive second layer, with resistivities no higher than 25 [Ωm], reaching up to 9 meters deep, and a resistive half space ($\rho > 200$ [Ωm]).

Table 4.1 shows a summary of the resistivity and contrast depth for all the models obtained. It indicates that both the shallow layer and the half-space have a great variability in their resistivity. The second layer on the other hand is better constrained only varying about 20 [Ωm] between all models.

Table 4.1: Resistivity and depth range for all the three layered models.

Layer	**Resistivity range [Ωm]**	**Depth range [m]**
Layer 1	19.3 - 305.1	1.5 - 6.2
Layer 2	6.9 - 25.7	4.7 - 9.1
Half-space	201.9 - 6356.8	—

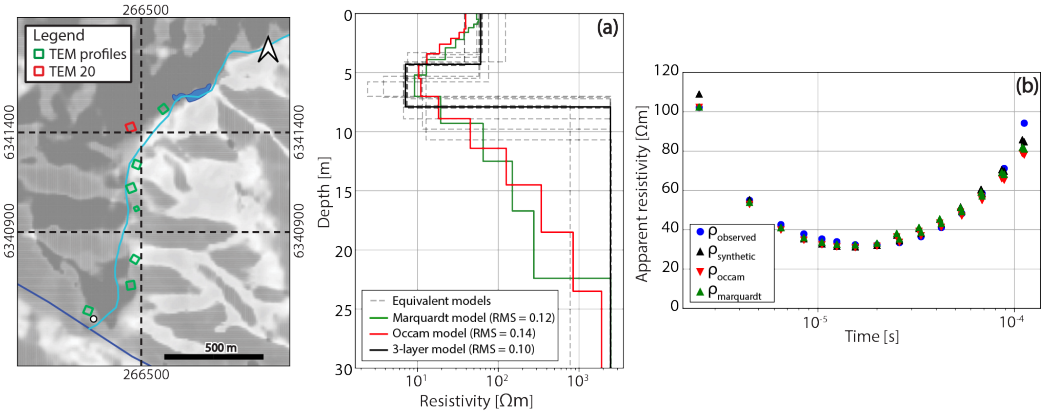

Figure 4.1: Figure a): all models obtained for station TEM 20, including the best fit three layer model (black line) and its equivalent models (gray dashed lines), the smooth occam model (red line) and the smooth Marquardt model (green line). Figure b): the observed apparent resistivity (blue dots) and modelled apparent resistivity (black triangles).

The Figure 4.3 (a) shows the map of the define TEM profile, and Figure 4.3 (b) displays the cross section of this profile. One of the predominant features observed is that based on the half-space resistivity, the stations can be divided into two groups: the stations TEM 7 and TEM 9, in the center of the profile present a half-space resistivity of around 200 [Ωm], and the rest of the stations (TEM 5, TEM 13 and TEM 3), located in the edges of the profile have a half-space resistivity higher than 1000 [Ωm]. Another feature of the profile, is the width of the intermediate layer, in the stations TEM 5 and TEM 3, in the edges of the profile, this layer reaches its minimum width. In the three center stations this with is higher, reaching its maximum value of about 20 meters in station TEM 13.

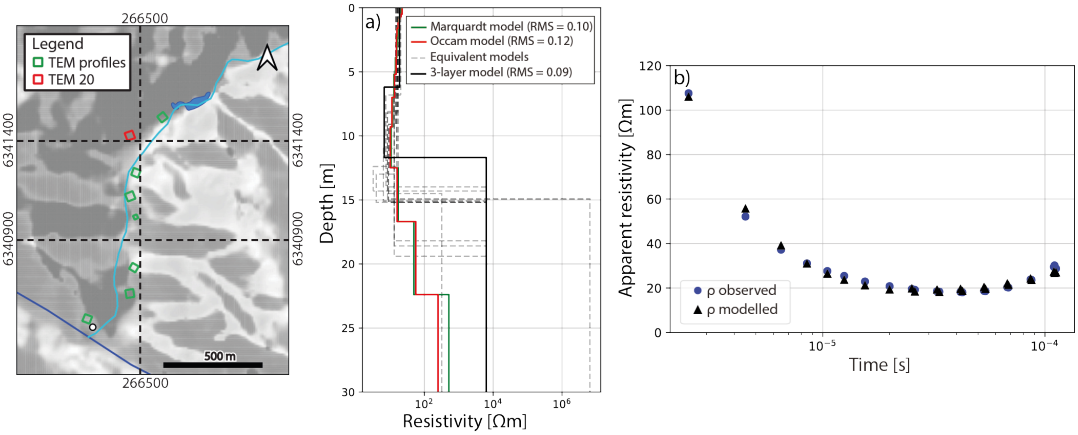

Figure 4.2: Figure a): all models obtained for station TEM 3, including the best fit three layer model (black line) and its equivalent models (gray dashed lines), the smooth occam model (red line) and the smooth Marquardt model (green line). Figure b): the observed apparent resistivity (blue dots) and modelled apparent resistivity (black triangles).

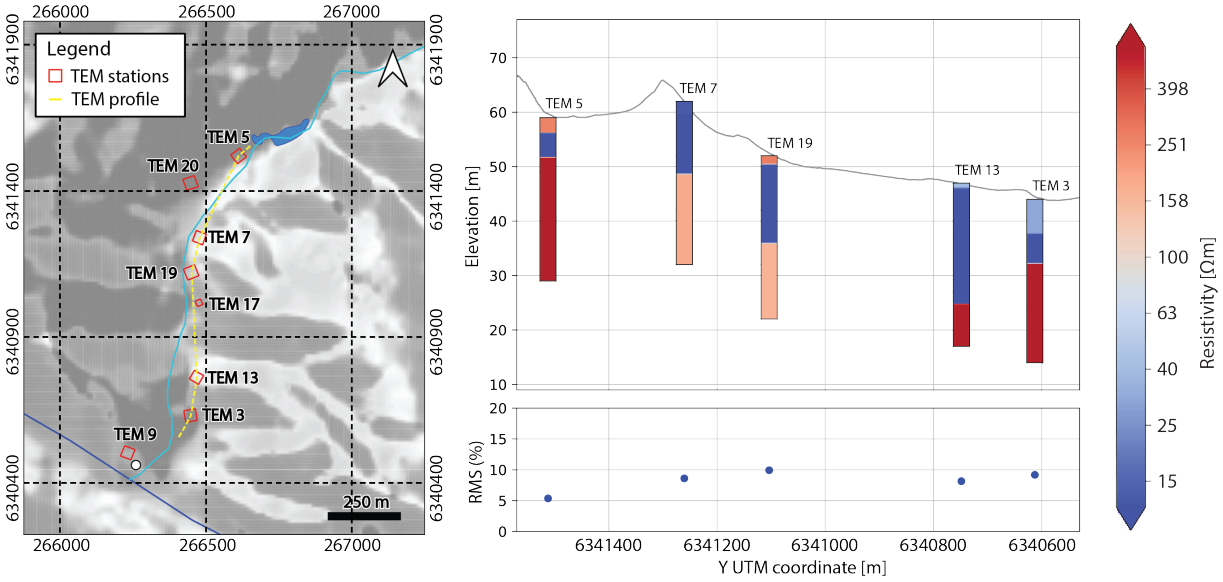

Figure 4.3: Left: Map showing the defined TEM profiles. Upper right: cross section of the TEM profile, showing the resistivity values of all the TEM stations included in the profile. Lower right: RMS of each profile.

4.2. Electrical Resistivity Tomography (ERT)

The Figure 4.4 shows the resistivity sections obtained for profiles ERT 10 and ERT 12, respectively. These profiles were chosen as representative of the two structures present in most profiles. On one hand, the profile ERT 10 shows a clear decrease of resistivity with depth, going from values higher than 1000 [Ωm] to values around 50 [Ωm]. Profile ERT 12 on the other hand, is much more conductive. One of the main features of this profile, is the conductive plume seen between 30 and 40 meters, that has resistivity values smaller than 10 [Ωm] and extends downwards. These plumes are also present in other profiles (Figures B.9 and B.10).

The Figure 4.5 corresponds to a boxplot, showing the quartiles of all ERT profiles. From this figure, three distinct groups can be defined. The first group is formed by the profiles ERT 2, ERT 4 and ERT 10. These profiles have a median value of around 100 [Ωm], and are all located in parts of the the BGVM that are not irrigated. The second group is made by the profiles ERT 7 and ERT 8, and have a median value of 40 [Ωm]. The profiles ERT 11 and ERT 12 form the third group, this is the most conductive of all, with a median resistivity of approximately 20 [Ωm], this last group has a very small dispersion.

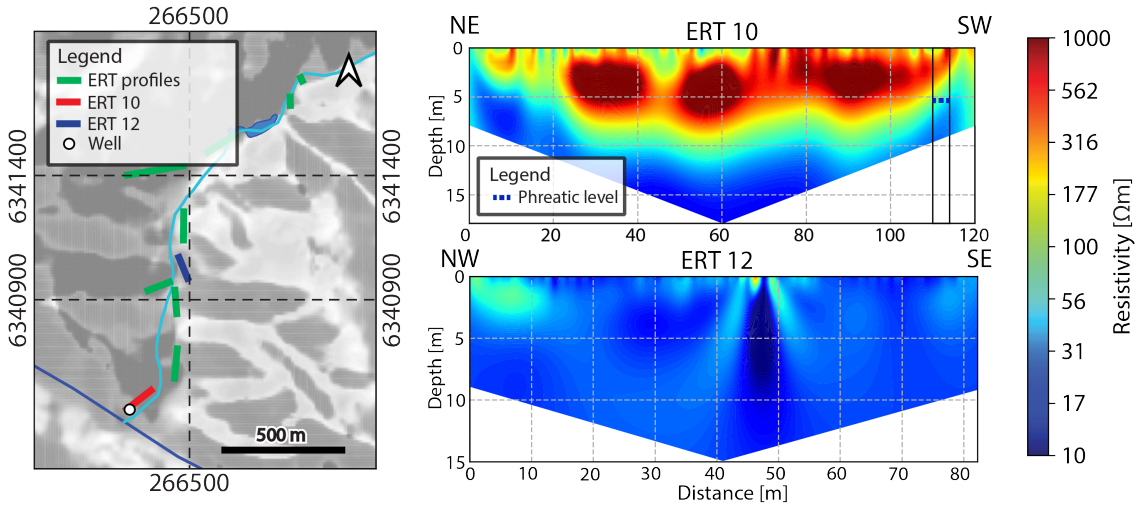

Figure 4.4: Resistivity model obtained for profile ERT 12 (map shown in Figure 2.12)

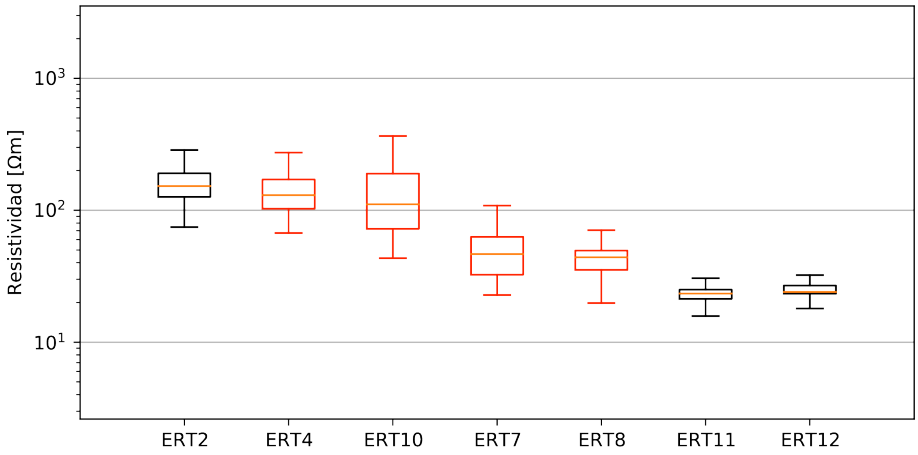

Figure 4.5: Boxplot of ERT profiles. Red boxes indicate profiles with a clear vertical gradient of the resistivity, and black boxes indicate profiles with no clear vertical gradient.

4.3. Gravimetry

4.3.1. Surface anomaly

The surface anomaly obtained is shown in Figure 4.6, and ranges approximately between -1 [mGal] and 1 [mGal]. There is a clear two zone distinction in the study area: a northern zone with an overall positive gravimetric anomaly, and a southern zone with an overall negative anomaly. This is consistent with surface observations of basement outcrops towards the positive anomaly areas.

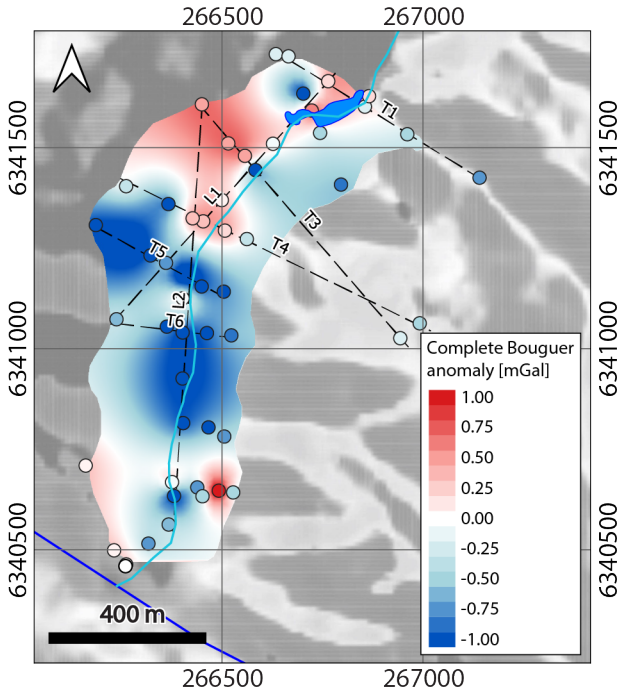

Figure 4.6: Surface gravimetric anomaly, presented as an interpolation and as the discrete values obtained for each station. The profiles modeled are shown in a black dashed line.

4.3.2. Profile models

Even though there was no stratigraphic information, an attempt was made to model seven gravimetric profiles, two longitudinal and five transversal (L and T profiles respectively in figure 4.6). The profiles were modelled considering a background density of 2670 [kg/cm^3], a sediment density of 2000 [kg/cm^3], a density of intrusive bodies of 2970 [kg/cm^3] and a fracture basement density of 2370 [kg/cm^3]. This values were chosen from the density ranges shown in Figure 2.3.

The intention was always trying to model the profile with as little elements as possible. First, a sedimentary layer was introduced in the model. If the profile presented positive anomalies, it was also necessary to include one or high density bodies. In a few profiles, an abrupt change in the gravity anomaly made it impossible to reproduce the data with only this types of bodies without geologically unrealistic structures, and thus the third structure (considered as fractured basement) was used.

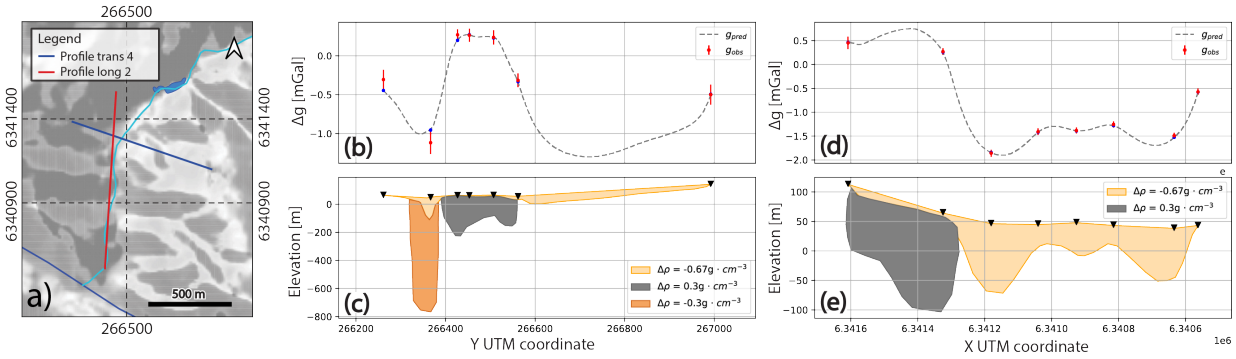

Figure 4.7: Forward models obatained for profiles trans 4 (figure (b)), and long 2 (figure (d)) with their respective gravimetric responses (figures (a) and (c)). For figures (a) and (c), red dots are the measured residual gravity with its their errorsm blue dots are the predicted gravimetric response above the gravimetric stations, and the dashed gray line is the continuous predicted gravimetric anomaly.

The Figure 4.7 shows two forward models, obtained for profiles trans 4 and long 2. The profile trans 4 was one of those where it was necessary to use the three types of bodies, to account for the abrupt variation of the anomaly. The profile long 2 had a simpler structure, the possitive anomaly in the northern part of the profile made it necessary to include an intrusive body, and the rest of the profile was modelled with only a sedimentary layer.

Chapter 5

Interpretation and discussions

5.1. Sediment thickness estimate

Based on TEM and gravity measurements, a sediment thickness was calculated. In the gravimetric profiles, the thickness was always estimated as the depth where the sediment layer finished. In the case of TEM, it was considered that only the profiles where the half-space had a resistivity higher than 1000 [Ωm] reached the basement.

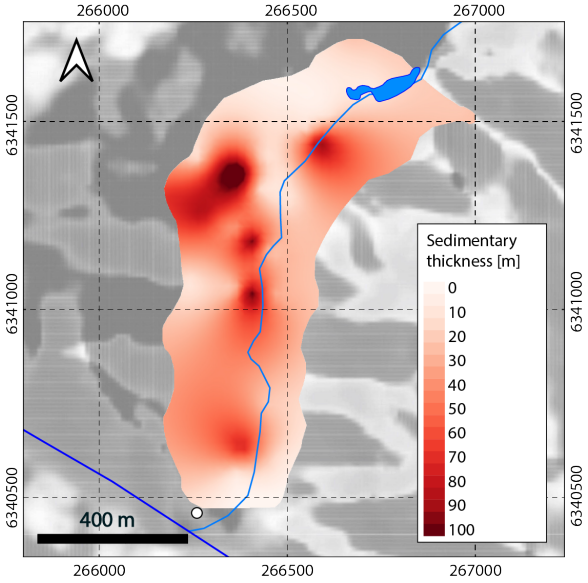

Figure 5.1: Sediment thickness interpolated in the study area, also showing the Linneo Lagoon (blue polygon), the Olivar stream (lightblue line) and the Marga Marga stream (blue line).

The figure 5.1 shows a generally shallow sediment layer, with five zones where the sediment reaches greater depths (between 60 and 120 meters), these zones are referred to in the literature as depocenters. Four of these depocenters are located around the Olivar stream, and one is located further west. This distribution of depocenters around the stream could correlate with sediments transported by the stream. Depocenters of this magnitude in such a small basin doesn't have precedents in the literature. This is one of the main reasons why the proposed geological model includes more structures (eg. fractured basement), to account for these unrealistic structures.

5.2. Water Table depth estimate

To estimate the water table depth, all inverted TEM and ERT measurements were used. For TEM, it was assumed that the groundwater was found at the depth at which the intermediate conductive layer begun (Figures 4.1 and 4.2), as some authors have shown that a conductive layer in TEM models show a good correlation with the water table (Viguier et al., 2018; Yáñez et al., 2015). The estimation from ERT profiles wasn't as straight forward, and two different approaches were taken, but both considered the horizontal average of the profile resistivity (figure 5.2).

The first approach, named resistivity method, was trying to find a representative resistivity for the aquifer. In profile ERT 10, a horizontal line was projected at the depth were the water table was seen (5.4 [m]) and the resistivity section beneath it was averaged, obtaining a resistivity of 173 [Ωm], that falls within the resistivity range of fresh water according to the literature (Figure 2.1). Then, the groundwater depth in each profile was estimated as the median value between the intersection of the 173 [Ωm] line and area $\rho_{avg} \pm$ std, as can be seen in the figure 5.2 (b). In profile ERT 4 the 173 [Ωm] straight line coincides at all depths with this area, and so only for this case, the water table depth was considered as the intersection of ρ_{avg} with the 173 [Ωm]. For this method two profiles (ERT 11 and ERT 12), presented resistivity values below the assumed aquifer resistivity, and so it was not possible to associate a water table depth. For profile ERT 10, this method results in a water table depth of 6.5 meters.

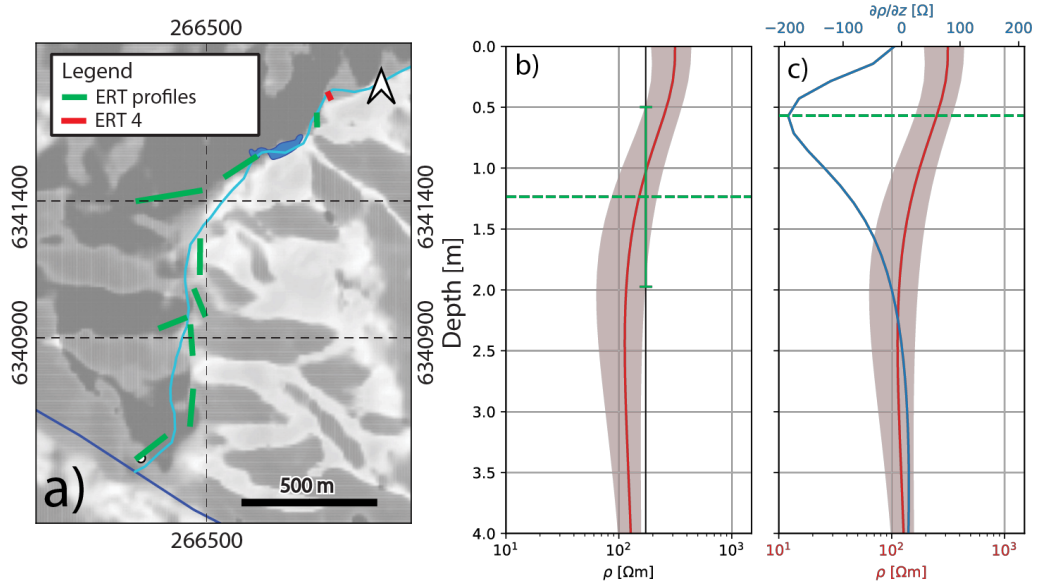

Figure 5.2: Comparison of both methods for profile ERT 4. Figure a) Groundwater depth estimation using the resistivity approach, both edges of the continuous green line indicate the intersection between the resistivity of the aquifer (173 [Ωm]) and the resistivity profile ± its standard deviation. Figure b) Groundwater depth estimation using the gradient method, the blue line is the gradient of the 1D resistivity curve.

The second method, referred to as the gradient method, consisted in calculating the gra-

dient of the 1D resistivity curve, finding its minimum value, and associating it to the groundwater depth (Figure 5.2 (a)). Unlike the previous method, this allows to find a water table depth for every inverted profile. In this case, the water table depth for the profile ERT 10 is 5 meters. A comparison of both methods for the profile ERT 4 is shown in Figure 5.2. In both approaches used, results indicate a water table depth between 0.5 and 6 meters, consistent with the well observation.

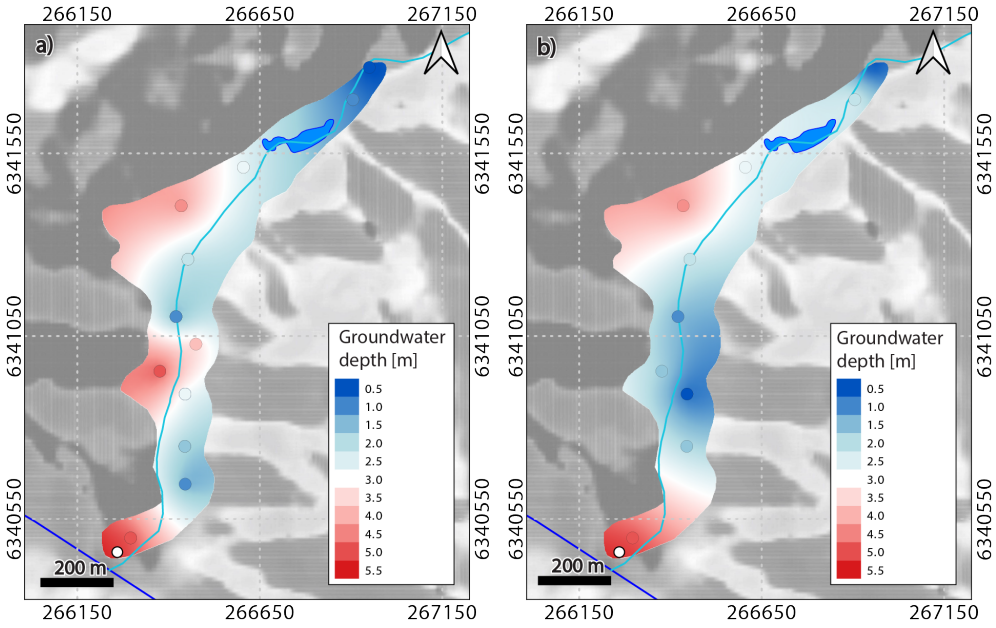

Figure 5.3: Figure a) Interpolation of the groundwater depth estimation using the gradient method. Figure b) Interpolation of the groundwater depth using the resistivity method.

As can be seen in the Figure 5.3, the results of both methods are generally consistent, the main difference is observed towards the middle of the study area, where the gradient method presents an intermediate zone where the water table deepens, whereas the resistivity method shows a smoother and shallower water table, until the southernmost area of the study zone. Regarding the water table depth measured in the well (5.4 [m]), the gradient method presents a closer result (5 [m]), than the resistivity method (6.5 [m]). Overall, it is considered that the resistivity method performs better, given that there is no reason to expect an increase in the water table depth towards the center of the studied area.

5.3. Comparison of geophysical methods

To validate the individual results, comparisons between different measurements were done. A comparison between profile ERT 11 and station TEM 3 is seen in Figure 5.4. This Figure shows that both methods present a reduction of the resistivity in a similar depth ($\sim$ 5 meters), further deep, the TEM station shows an increase in the resistivity that is also observed, but in a smaller degree, in the ERT profile, between 10 and 15 meters of depth.

This difference observed between methods is due to the different way in which both methods estimate the subsurface's resistivity (detailed in sections 2.3 and 2.4). According to Albouy et al. (2001), the ERT method is sensitive to the so called transverse resistivity, that

is, the product of thickness and resistivity, whereas TEM is sensitive to the thickness of the layers. Furthermore, the current in the ERT method tends to run parallel to low resistivity layers, making it difficult to reach greater depths when a conductive structure is found. Christiansen et al. (2007) states that TEM poorly resolves shallow and resistive layers, and that ERT has particularly good resolution closer to the surface, decreasing downwards.

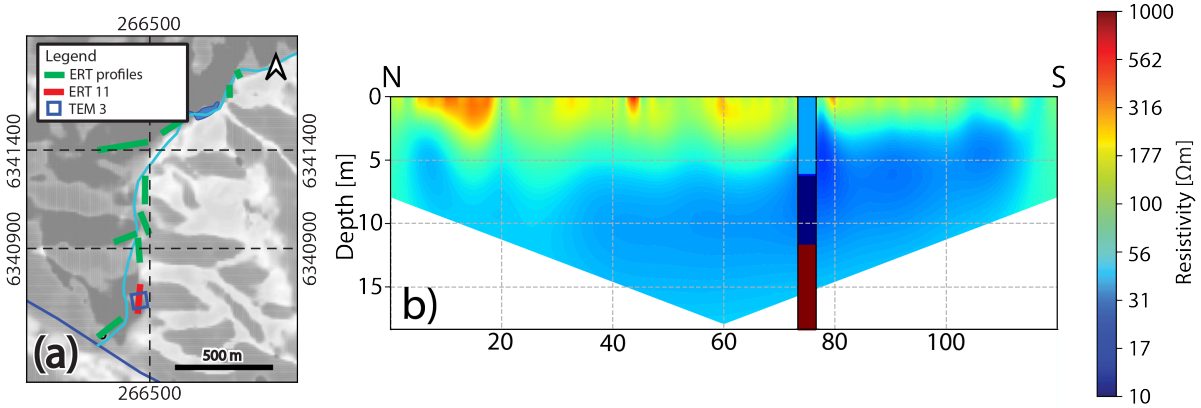

Figure 5.4: ERT 11 profile and TEM 3 station, using the same colorbar scale, saturated to 100 [Ωm].

Figure 5.5 shows the comparison between the gravimetric profile long 2 and the TEM stations TEM 20 and TEM 19. Here, it can be seen that the presence of a high density body and a very resistive half-space of station TEM 20 coincide. On the other hand, station TEM 19 indicates that there is a change in the resistivity of the sedimentary layer, suggesting that this low density body might include more than one structure. From this comparisons, we can classify the subsurface in four structres, based on their density and resistivity: (1) **low density, variable resistivity**; (2): **low density, low resistivity**; (3): **low density, medium resistivity** and (4): **high density, high resistivity**. The bodies (1) and (2), correspond to unsaturated and saturated sediments, respectively.

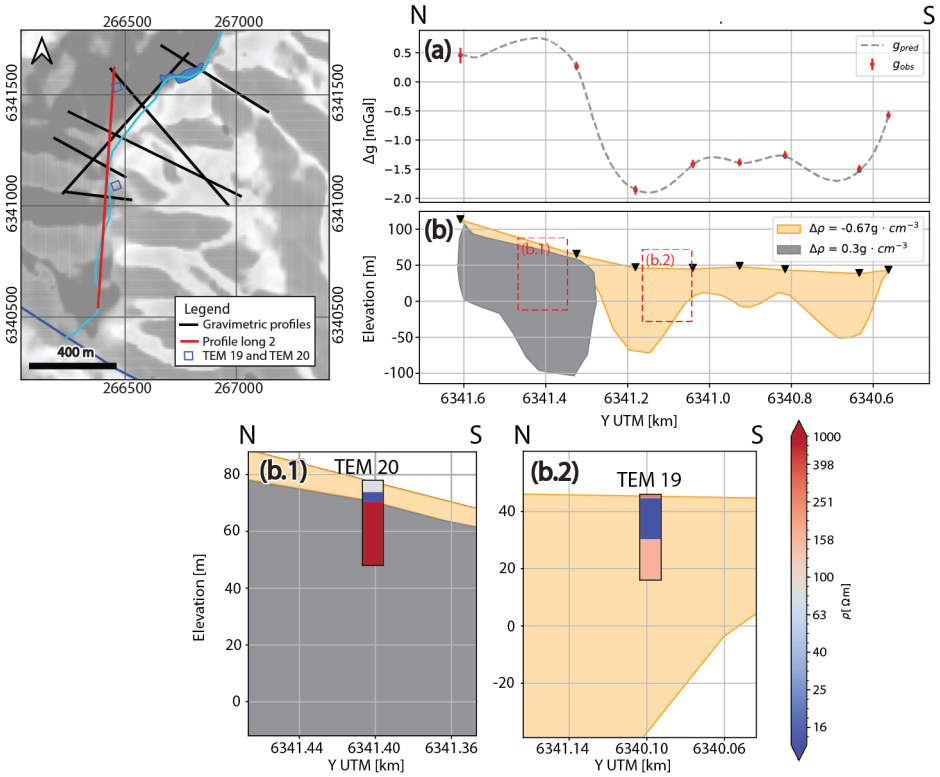

Figure 5.5: Gravimetric profile long 2 and TEM stations

5.4. Geologic and hydrogeologic model

In this section, a hydrogeologic model in proposed based on the geophysical observations. Figure 5.5 shows the joint results of the gravimetric profile long 2 and TEM stations TEM 20 and TEM 19. As mentioned before, the high resistivity half space ($>$ 1000 [Ωm]) of the station TEM 20 coincides with a high density structure defined from gravimetry, and the medium resistivity half-space ($\sim$ 200 [Ωm]) of station TEM 19, falls within the low density area. Moreover, Figure 4.3 shows that both TEM 7 and TEM 19 stations present this medium resistivity half-space towards the center of the study area. This low density and medium resistivity structure is interpreted as a highly fractured basement due to weathering. Indeed, this supposition is supported by previous studies that have found similar resistivities in granites (Krishnamurthy et al. (2004); Dewandel et al. (2006) Figure 6), and by field observations (Figure 3.3, Picture a.1). Furthermore, the study of Martín (2023), infers the same kind of structure in a similar intramontane basin: the Catemu Valley.

Some profiles, according to the density models, present a sediment thicknesses of up to $\sim$ 150 [m]. This depth of sedimentary infill makes little geological sense and does not agree with other studies that observe a sediment thicknesses only a few times deeper, in areas that are tens of times bigger that the BGVM watershed in Chile (Figueroa et al., 2021; Yáñez et al., 2015; Marti et al., 2023; Martín, 2023; González et al., 2018) and other countries (Özalaybey et al., 2011). Due to this, another structure must be present to be able to explain for these short-extension mass deficits. An appropriate structure to account for these

are low density areas associated with shallow crustal faults, coherent with the active tectonic setting of central Chile (Angermann et al., 1999), and the mapped faults next to the study area seen in Figure 3.1 (de Geología y Minería et al., 1996). This would mean that there is fractured basement due to weathering and tectonic, much like the models proposed by Wyns et al. (2004) and (Dewandel et al., 2006). Recently Marti et al. (2023) also proposed fractured basement in gravimetric models.

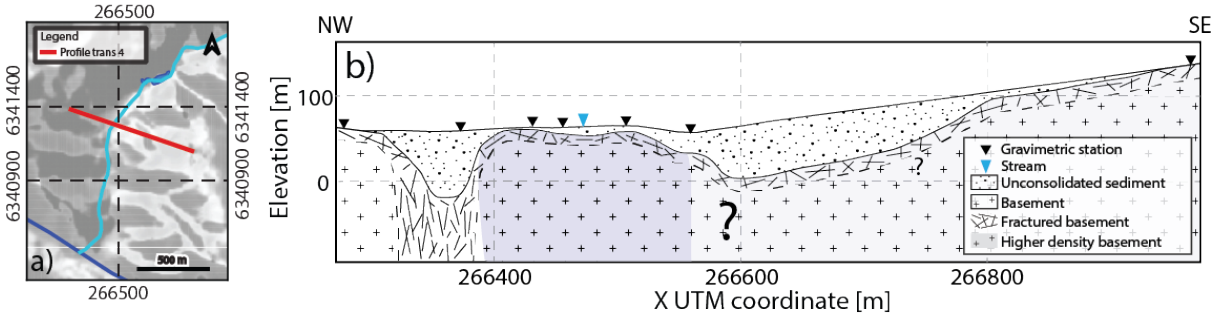

Figure 5.6: Geological interpretation of gravimetric profile trans 4

The Figures 5.6, 5.7 and 5.8 show the geological models proposed for the gravimetric profiles trans 4, trans 6 and long 2, and Figure 5.9 shows a hydrogeological model from the TEM profile. Lachassagne et al. (2011) affirms that the fractures due to weathering of a plutonic rock must be evenly distributed, and so this interpreted layer is extended to all the profiles. Both trans 4 and trans 6 models include interpreted tectonic fractures, because otherwise, the gravimetric anomaly would have to be modelled with an unrealistic sediment thickness.

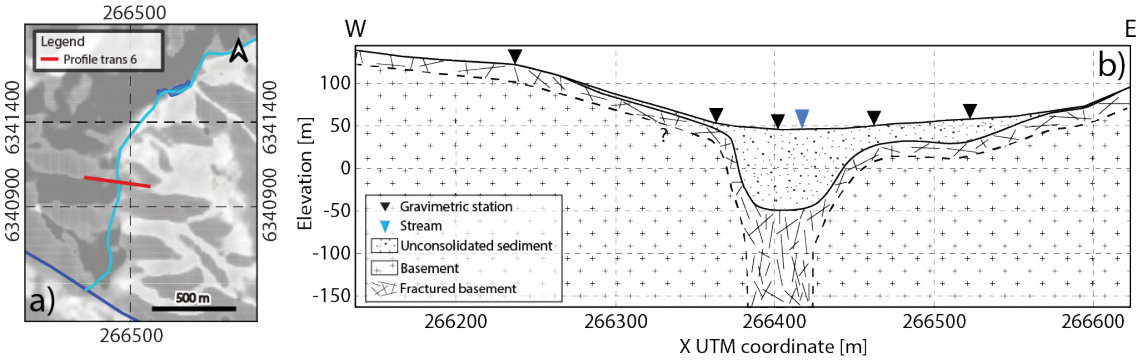

Figure 5.7: Geological interpretation of gravimetric profile trans 6

From the TEM profile, a hydrogeologic model is proposed. The intermediate conductive layer of the TEM models are interpreted as saturated sediment, as mentioned in the section 6.2. The half-spaces with intermediate resistivity are interpreted as saturated fractured basement. The interaction type between the stream and groundwater remains unresolved. The profile crosses the stream once, between stations TEM 5 and TEM 7, and in order to be a connected system, the water table must reach the surface in this point (Brunner et al., 2009). The fact that station TEM 7 has the lowest resistivity contrast between the first two layers could indicate a particularly low water table depth, but more information is required to define this system as connected, disconnected or transitional.

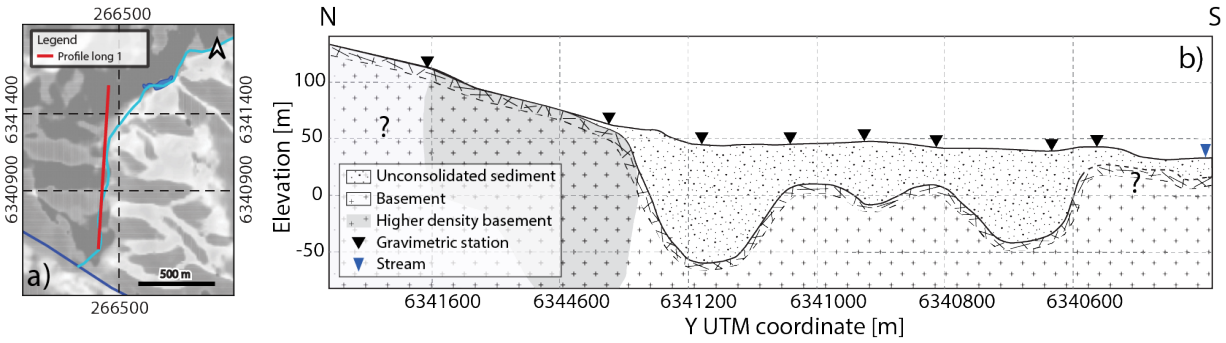

Figure 5.8: Geological interpretation of gravimetric profile long 2

Regarding the recharge site deliniation, while there are some studies that use geophysical methods for these purposes (Sendrós et al., 2020), most of them complement these observations with other measurements, such as geochemistry (Daesslé et al., 2014). Nevertheless, the low resistivities of the profiles located in irrigated zones (profile ERT 12 in Figure 4.4) are indicative of infiltration form irrigation. Furthermore, none of the geophysical measurements indicate any structures that might hinder the infiltration process, such as clay lenses. Yáñez et al. (2015) shows that the basement depth can correlate with the phreatic level. In this study, this occurs only for the biggest depocenter (the second one from north to south, Figure 5.1), where we see also a deepening in the groundwater depth (Figure 5.2). It is then proposed that this depocenter is the best choice to perform the artificial recharge, given that the deep groundwater table and basement allows a bigger volume of stored water.

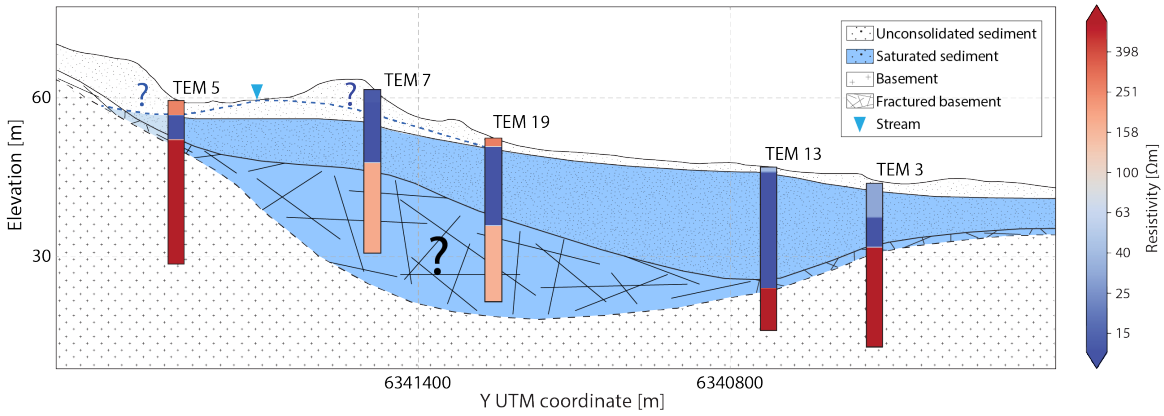

Figure 5.9: Hydrology model of TEM profile (Figure 4.3)

The Figure 5.10 displays the map projections of all high density basement features and tectonic fracture structures defined in the conceptual models. All high density basement inferences are concentrated to the NW of the study area, and so they might be explained with one big intrusive (named B1 in the Figure). The four fault features proposed in the geological models, can be divided into two lineaments: L1, with a NE-SW orientation that coincides with an observed fault NE of the study area, and L2 with a N-S orientation, that runs parallel to the infered fault that delimits the eastern edge of the intrusive paleozoic unit. A broader map showing mapped and inferred faults can be found in the annex.

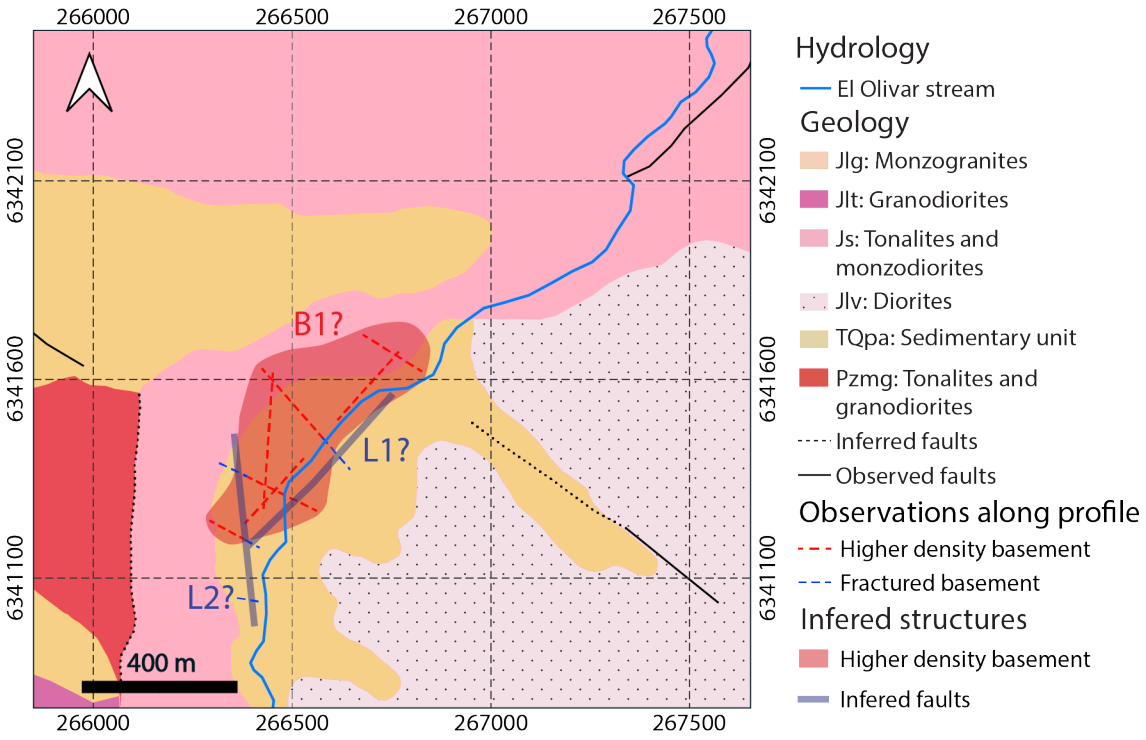

Figure 5.10: Inferred structures from the geological models based on the density models. The red dashed lines represent the sections of the profiles where the high density basement was observed, and the blue dashed lines are the areas where the tectonic fractures were observed. The red semi transparent polygon represent a possible subsurface continuous dense basement, and the two semi transparent blue lines are two possible fault lineaments.

Chapter 6

Conclusions

Given the interest of the research consortium CAPTA in the BGVM watershed, an initial geophysical study was carried out to gain insights about the hydrologic regime and the underlying geology. Results of TEM and ERT show a decrease of the electrical resistivity within the first 7 meters, that is attributed to the water table. Deeper, the results of both methods differ, ERT shows a more or less constant low resistivity values, and TEM indicates an increase in the resistivity. This can be caused by the different physical mechanisms of these methods, as has been reported by some authors (Raiche et al., 1985; Albouy et al., 2001). This increase in resistivity can be divided in two: some TEM stations show an increase of 1000 [Ωm] or higher, and some stations show an increase up to around 200 [Ωm].

The gravity anomaly obtained showed two main areas, a positive anomaly in the northern part of the study area, and a negative anomaly in the southern part (Figure 4.6). Seven profiles were modeled with the Won-Bevis forward algorithm (Won & Bevis, 1987), using three density constrasts: (1) $\Delta\rho$ = -670 [kg/m^3] for the sediment, (2) $\Delta\rho$ = -300 [kg/m^3] for fractured basement, and (3) $\Delta\rho$ = 300 [kg/m^3].

With the joint analysis of resistivity and density results, it was possible to define four different features:

- Low density, low to medium resistivity: this is the shallowest structure observed, and is interpreted as unsaturated sediment, with different degrees of moisture.
- Low density, low resistivity: this is interpreted as saturated sediment.
- Low density, medium resistivity: this is interpreted as saturated highly fractured basement, due to either tectonic or weathering processes.
- High density, high resistivity: this unit is assumed to be either normal or high density basement.

These results suggest that the groundwater present in the study area is supported by both sediments and fractured hard rock mediums.

Regarding the defined objectives, the final conclusions are presented here. It was possible to estimate the groundwater depth from the TEM and ERT resistivity models. For ERT models, two different methods were used (resistivity and gradient), that showed generally

consistent results between them. The basement depth was inferred from both TEM and gravity measurements, but the interpreted presence of fractured basement made the completion of this objective more complex than originally anticipated. Finally, some general ideas can be said about the recharge site delineation. The conductive profiles are indicative that the water in the BGVM infiltrates downwards when irrigated, suggesting that the infiltration rate is appropriate for the artifitial recharge. The selected site for artifitial aquifer recharge is the second depocenter from north to south, because in that area a deepening of both the basement and water table are observed, indicating that this zone could store the biggest amount of water in the BGVM.

It is noted that more studies are necessary to thoroughly understand the geology and the hydrogeology of the area. It is specially important to perform direct geological observations to validate the results obtained in this work. Other useful works could be stream flow measurements in different points in the watershed (Marti et al., 2023), a denser grid of gravimetric measurements, in order to perform a 3D inversion (González et al., 2018; Martín, 2023), a magnetic survey to delineate structures (Marti et al., 2023) or to model the sedimentary infill (Ibraheem et al., 2018) and longer ERT profiles that can be directly compared with gravimetric measurements (Figueroa et al., 2021; Marti et al., 2023).

Bibliography

Albouy, Y., Andrieux, P., Rakotondrasoa, G., Ritz, M., Descloitres, M., Join, J.-L., & Rasolomanana, E. (2001). Mapping coastal aquifers by joint inversion of dc and tem soundings-three case histories. *Groundwater*, *39*(1), 87–97.

Angermann, D., Klotz, J., & Reigber, C. (1999). Space-geodetic estimation of the nazca-south america euler vector. *Earth and Planetary Science Letters*, *171*(3), 329–334.

Archie, G. E. (1942). The electrical resistivity log as an aid in determining some reservoir characteristics. *Transactions of the AIME*, *146*(01), 54–62.

Asten, M. W. (1987). Full transmitter waveform transient electromagnetic modeling and inversion for soundings over coal measures. *Geophysics*, *52*(3), 279–288.

Binley, A., Hubbard, S. S., Huisman, J. A., Revil, A., Robinson, D. A., Singha, K., & Slater, L. D. (2015). The emergence of hydrogeophysics for improved understanding of subsurface processes over multiple scales. *Water resources research*, *51*(6), 3837–3866.

Bisnath, S., & Collins, P. (2012). Recent developments in precise point positioning. *Geomatica*, *66*(2), 103–111.

Blanco, B. (2016). *Análisis de las variaciones de resistividad eléctrica utilizando transiente electromagnético en la cuenca de santiago* (Unpublished master's thesis). Universidad de Chile.

Boisier, J. P., Rondanelli, R., Garreaud, R. D., & Muñoz, F. (2016). Anthropogenic and natural contributions to the southeast pacific precipitation decline and recent megadrought in central chile. *Geophysical Research Letters*, *43*(1), 413–421.

Bonnefoy-Claudet, S., Baize, S., Bonilla, L. F., Berge-Thierry, C., Pasten, C., Campos, J., ... Verdugo, R. (2009). Site effect evaluation in the basin of santiago de chile using ambient noise measurements. *Geophysical Journal International*, *176*(3), 925–937.

Bouwer, H., Back, J. T., & Oliver, J. M. (1999). Predicting infiltration and ground-water mounds for artificial recharge. *Journal of Hydrologic Engineering*, *4*(4), 350–357.

Brunet, P., Clément, R., & Bouvier, C. (2010). Monitoring soil water content and deficit using electrical resistivity tomography (ert)–a case study in the cevennes area, france. *Journal of Hydrology*, *380*(1-2), 146–153.

Brunner, P., Cook, P. G., & Simmons, C. T. (2009). Hydrogeologic controls on disconnection between surface water and groundwater. *Water Resources Research*, *45*(1).

Carmichael, R. S. (2017). *Practical handbook of physical properties of rocks and minerals (1988)*. CRC press.

Chen, J., Hubbard, S., & Rubin, Y. (2001). Estimating the hydraulic conductivity at the

south oyster site from geophysical tomographic data using bayesian techniques based on the normal linear regression model. *Water Resources Research*, *37*(6), 1603–1613.

Christiansen, A. V., Auken, E., Foged, N., & Sørensen, K. I. (2007). Mutually and laterally constrained inversion of cves and tem data: a case study. *Near Surface Geophysics*, *5*(2), 115–123.

Christiansen, A. V., Auken, E., & Sørensen, K. (2006). The transient electromagnetic method. In *Groundwater geophysics: a tool for hydrogeology* (pp. 179–225). Springer.

Constable, S. C., Parker, R. L., & Constable, C. G. (1987). Occam's inversion: A practical algorithm for generating smooth models from electromagnetic sounding data. *Geophysics*, *52*(3), 289–300.

Daesslé, L., Pérez-Flores, M., Serrano-Ortiz, J., Mendoza-Espinosa, L., Manjarrez-Masuda, E., Lugo-Ibarra, K., & Gómez-Treviño, E. (2014). A geochemical and 3d-geometry geophysical survey to assess artificial groundwater recharge potential in the pacific coast of baja california, mexico. *Environmental earth sciences*, *71*, 3477–3490.

Danielsen, J. E., Auken, E., Jørgensen, F., Søndergaard, V., & Sørensen, K. I. (2003). The application of the transient electromagnetic method in hydrogeophysical surveys. *Journal of applied geophysics*, *53*(4), 181–198.

Darcy, H. (1856). *Les fontaines publiques de la ville de dijon: exposition et application des principes à suivre et des formules à employer dans les questions de distribution d'eau* (Vol. 1). Victor dalmont.

de Geología y Minería, C. S. N., Wall, R., Gana, P., & Gutiérrez, A. (1996). *Mapa geológico del área de valparaíso-curacaví, regiones de valparaíso y metropolitana*. Servicio Nacional de Geología y Minería.

Dewandel, B., Lachassagne, P., Wyns, R., Maréchal, J.-C., & Krishnamurthy, N. (2006). A generalized 3-d geological and hydrogeological conceptual model of granite aquifers controlled by single or multiphase weathering. *Journal of hydrology*, *330*(1-2), 260–284.

Domenico, P., & Schwartz, F. (1998). Physical and chemical hydrogeology, 2nd edn john wiley & sons. *New York*.

Fetter, C. W. (2018). *Applied hydrogeology*. Waveland Press.

Figueroa, R., Viguier, B., Taucare, M., Yáñez, G., Arancibia, G., Sanhueza, J., & Daniele, L. (2021). Deciphering groundwater flow-paths in fault-controlled semiarid mountain front zones (central chile). *Science of The Total Environment*, *771*, 145456.

Garreaud, R. D., Alvarez-Garreton, C., Barichivich, J., Boisier, J. P., Christie, D., Galleguillos, M., ... Zambrano-Bigiarini, M. (2017). The 2010–2015 megadrought in central chile: Impacts on regional hydroclimate and vegetation. *Hydrology and earth system sciences*, *21*(12), 6307–6327.

Garreaud, R. D., Boisier, J. P., Rondanelli, R., Montecinos, A., Sepúlveda, H. H., & Veloso-Aguila, D. (2020). The central chile mega drought (2010–2018): a climate dynamics perspective. *International Journal of Climatology*, *40*(1), 421–439.

González, F. A., Maksymowicz, A., Díaz, D., Villegas, L., Leiva, M., Blanco, B., ... Bonvalot, S. (2018). Characterization of the depocenters and the basement structure, below the central chile andean forearc: A 3d geophysical modelling in santiago basin area. *Basin*

Research, *30*(4), 799–815.

Hinze, W. J., Von Frese, R. R., Von Frese, R., & Saad, A. H. (2013). *Gravity and magnetic exploration: Principles, practices, and applications*. Cambridge University Press.

Ibraheem, I. M., Gurk, M., Tougiannidis, N., & Tezkan, B. (2018). Subsurface investigation of the neogene mygdonian basin, greece using magnetic data. *Pure and Applied Geophysics*, *175*, 2955–2973.

Johnson, T. C., Slater, L. D., Ntarlagiannis, D., Day-Lewis, F. D., & Elwaseif, M. (2012). Monitoring groundwater-surface water interaction using time-series and time-frequency analysis of transient three-dimensional electrical resistivity changes. *Water Resources Research*, *48*(7).

Krishnamurthy, N., Kumar, D., Negi, B., Jain, S., & Ahmed, S. (2004). *Resistivity investigations for identifying fractured aquifers in a granitic terrain.* Hyderabad.

Lachassagne, P., Wyns, R., & Dewandel, B. (2011). The fracture permeability of hard rock aquifers is due neither to tectonics, nor to unloading, but to weathering processes. *Terra Nova*, *23*(3), 145–161.

Longman, I. (1959). Formulas for computing the tidal accelerations due to the moon and the sun. *Journal of Geophysical Research*, *64*(12), 2351–2355.

Lowrie, W., & Fichtner, A. (2020). *Fundamentals of geophysics*. Cambridge university press.

Madsen, K., Nielsen, H. B., & Tingleff, O. (2004). Methods for non-linear least squares problems.

Marquardt, D. W. (1963). An algorithm for least-squares estimation of nonlinear parameters. *Journal of the society for Industrial and Applied Mathematics*, *11*(2), 431–441.

Marti, E., Leray, S., Villela, D., Maringue, J., Yáñez, G., Salazar, E., ... others (2023). Unravelling geological controls on groundwater flow and surface water-groundwater interaction in mountain systems: a multi-disciplinary approach. *Journal of Hydrology*, 129786.

Martín, F. S. (2023). *Caracterización gravimétrica de la zona norte de la cuenca estero catemu: Análisis de un acuífero en roca fracturada* (Unpublished master's thesis). Universidad de Chile.

Miller, C. R., Routh, P. S., Brosten, T. R., & McNamara, J. P. (2008). Application of time-lapse ert imaging to watershed characterization. *Geophysics*, *73*(3), G7–G17.

Mireault, Y., Tétreault, P., Lahaye, F., Héroux, P., & Kouba, J. (2008). Online precise point positioning. *GPS world*, *19*(9), 59–64.

Montecinos, D. (2019). *Modelamiento geofísico de las esctructuras someras del sistema geotermal el tatio* (Unpublished master's thesis). Universidad de Chile.

Nabighian, M. N., & Macnae, J. C. (1991). Time domain electromagnetic prospecting methods. In *Electromagnetic methods in applied geophysics: Volume 2, application, parts a and b* (pp. 427–520). Society of Exploration Geophysicists.

Niwas, S., Tezkan, B., & Israil, M. (2011). Aquifer hydraulic conductivity estimation from surface geoelectrical measurements for krauthausen test site, germany. *Hydrogeology Journal*, *19*(2), 307.

Özalaybey, S., Zor, E., Ergintav, S., & Tapırdamaz, M. C. (2011). Investigation of 3-d basin structures in the izmit bay area (turkey) by single-station microtremor and gravimetric methods. *Geophysical Journal International*, *186*(2), 883–894.

Raiche, A., Jupp, D., Rutter, H., & Vozoff, K. (1985). The joint use of coincident loop transient electromagnetic and schlumberger sound to resolve layered structures. *Geophysics*, *50*(10), 1618–1627.

Robinson, D., Binley, A., Crook, N., Day-Lewis, F., Ferré, T., Grauch, V., ... others (2008). Advancing process-based watershed hydrological research using near-surface geophysics: A vision for, and review of, electrical and magnetic geophysical methods. *Hydrological Processes: An International Journal*, *22*(18), 3604–3635.

Samouëlian, A., Cousin, I., Tabbagh, A., Bruand, A., & Richard, G. (2005). Electrical resistivity survey in soil science: a review. *Soil and Tillage research*, *83*(2), 173–193.

Sendrós, A., Himi, M., Lovera, R., Rivero, L., Garcia-Artigas, R., Urruela, A., & Casas, A. (2020). Geophysical characterization of hydraulic properties around a managed aquifer recharge system over the llobregat river alluvial aquifer (barcelona metropolitan area). *Water*, *12*(12), 3455.

Slater, L. (2007). Near surface electrical characterization of hydraulic conductivity: From petrophysical properties to aquifer geometries—a review. *Surveys in Geophysics*, *28*, 169–197.

Sørensen, K. I., Auken, E., & Thomsen, P. (2000). Tdem in groundwater mapping—a continuous approach. In *Symposium on the application of geophysics to engineering and environmental problems 2000* (pp. 485–491).

Taucare, M., Daniele, L., Viguier, B., Vallejos, A., & Arancibia, G. (2020). Groundwater resources and recharge processes in the western andean front of central chile. *Science of the Total Environment*, *722*, 137824.

Viguier, B., Jourde, H., Yáñez, G., Lira, E. S., Leonardi, V., Moya, C. E., ... Lictevout, E. (2018). Multidisciplinary study for the assessment of the geometry, boundaries and preferential recharge zones of an overexploited aquifer in the atacama desert (pampa del tamarugal, northern chile). *Journal of South American Earth Sciences*, *86*, 366–383.

Ward, S. H. (1990). *Geotechnical an environmental geophysics: Volume i: Review and tutorial*. Society of Exploration Geophysicists.

Won, I., & Bevis, M. (1987). Computing the gravitational and magnetic anomalies due to a polygon: Algorithms and fortran subroutines. *Geophysics*, *52*(2), 232–238.

Wyns, R., Baltassat, J.-M., Lachassagne, P., Legchenko, A., Vairon, J., & Mathieu, F. (2004). Application of proton magnetic resonance soundings to groundwater reserve mapping in weathered basement rocks (brittany, france). *Bulletin de la Société géologique de France*, *175*(1), 21–34.

Yáñez, G., Muñoz, M., Flores-Aqueveque, V., & Bosch, A. (2015). Gravity derived depth to basement in santiago basin, chile: implications for its geological evolution, hydrogeology, low enthalpy geothermal, soil characterization and geo-hazards. *Andean Geology*, *42*(2), 147–172.

Annex A

Gravity

A.1. Table of measurements

Table A.1: Gravimetric measurements part 1

Station	Date	Time	Z UTM	Measurement [mGal]
1	2022/05/18	14:11:30	42.6	4613.0
2	2022/05/18	14:23:50	41.9	4613.4
4	2022/05/18	15:14:23	64.6	4611.7
6	2022/05/18	15:38:56	77.6	4608.7
7	2022/05/18	15:51:48	64.6	4612.3
11	2022/05/18	16:29:44	59.1	4613.2
8	2022/05/18	16:09:56	56.7	4613.3
10	2022/05/18	16:17:00	61.4	4613.1
12	2022/05/18	16:37:40	64.4	4612.4
15	2022/05/18	20:36:49	41.4	4612.9
16	2022/05/18	20:41:33	43.8	4612.6
17	2022/05/18	20:46:37	39.4	4612.6
18	2022/05/18	20:52:26	48.0	4612.7
20	2022/05/18	21:08:09	44.6	4612.8
21	2022/05/18	21:13:39	49.2	4612.3
22	2022/05/18	21:20:34	46.6	4613.1
23	2022/05/18	21:31:01	57.9	4612.9
24	2022/05/18	21:36:19	56.0	4612.1
41	2022/05/19	19:54:46	50.8	4613.5
25	2022/05/19	15:43:15	45.8	4612.1
26	2022/05/19	15:51:07	55.3	4612.2
27	2022/05/19	15:55:31	45.5	4612.4
30	2022/05/19	16:26:45	50.3	4611.8

Table A.2: Gravimetric measurements part 2.

Station	**Date**	**Time**	**Z UTM**	**Measurement [mGal]**
28	2022/05/19	16:01:05	46.1	4612.3
29	2022/05/19	16:19:35	48.0	4612.3
34	2022/05/19	17:27:00	57.7	4611.3
32	2022/05/19	17:02:30	55.7	4612.1
33	2022/05/19	17:17:11	51.0	4612.4
35	2022/05/19	17:38:12	57.3	4611.7
36	2022/05/19	17:47:16	47.4	4612.9
37	2022/05/19	17:51:45	54.5	4613.2
38	2022/05/19	18:01:26	49.6	4613.5
39	2022/05/19	18:15:37	60.2	4611.4
40	2022/05/19	19:42:38	68.0	4612.1
42	2022/05/19	20:27:52	65.7	4612.4
43	2022/05/19	20:35:02	66.9	4612.0
44	2022/05/19	20:41:40	57.3	4612.9
45	2022/05/19	20:56:29	58.8	4612.4
48	2022/05/19	21:26:04	88.9	4608.1
46	2022/05/19	21:06:03	61.1	4612.2
47	2022/05/19	21:16:55	78.6	4608.1
C8	2022/05/21	17:59:07	67.4	4611.5
C2	2022/05/21	15:38:43	128.0	4596.8
C3	2022/05/21	16:26:50	122.9	4598.7
C4	2022/05/21	16:46:24	86.86	4607.2
C5	2022/05/21	17:20:54	113.8	4603.9
C6	2022/05/21	17:33:39	138.2	4598.7
C7	2022/05/21	17:41:04	135.2	4599.1
C9	2022/05/21	19:35:03	67.5	4611.6
C1	2022/05/21	19:48:00	85.9	4606.1
C1	2022/05/21	20:39:25	153.4	4591.7
C1	2022/05/21	20:49:39	145.4	4593.2
C1	2022/05/21	21:08:46	114.7	4600.8

A.2. Map of measured elevations

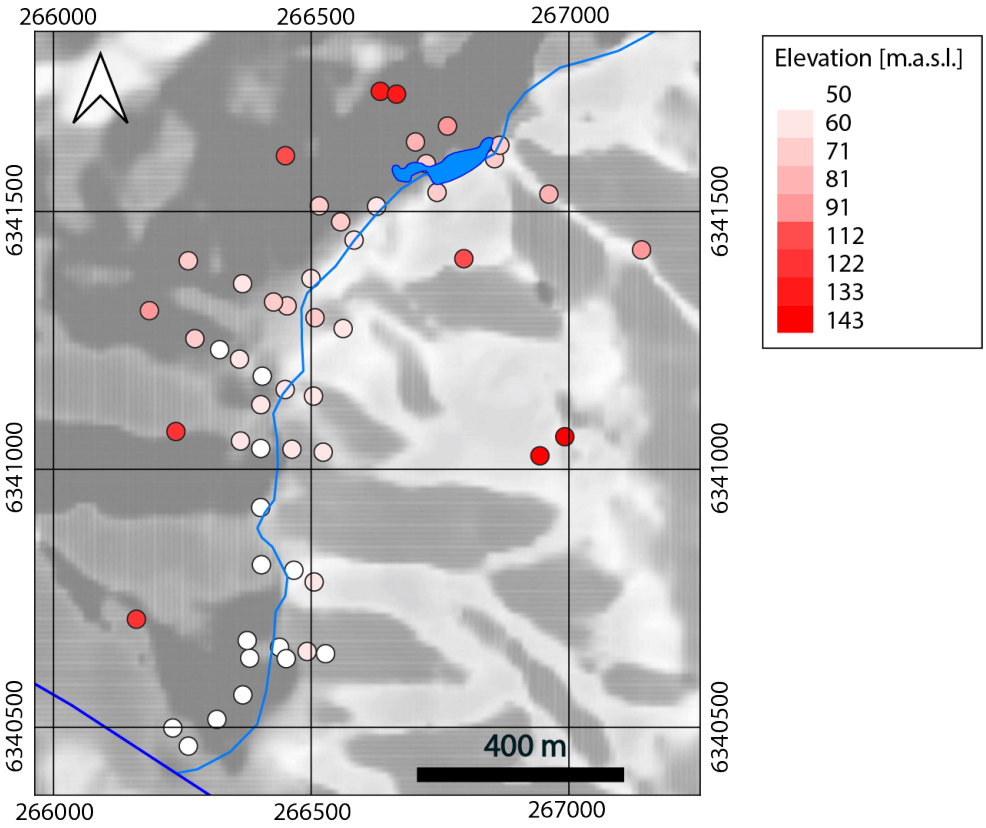

Figure A.1: Measured elevation from

A.3. Forward 2D models

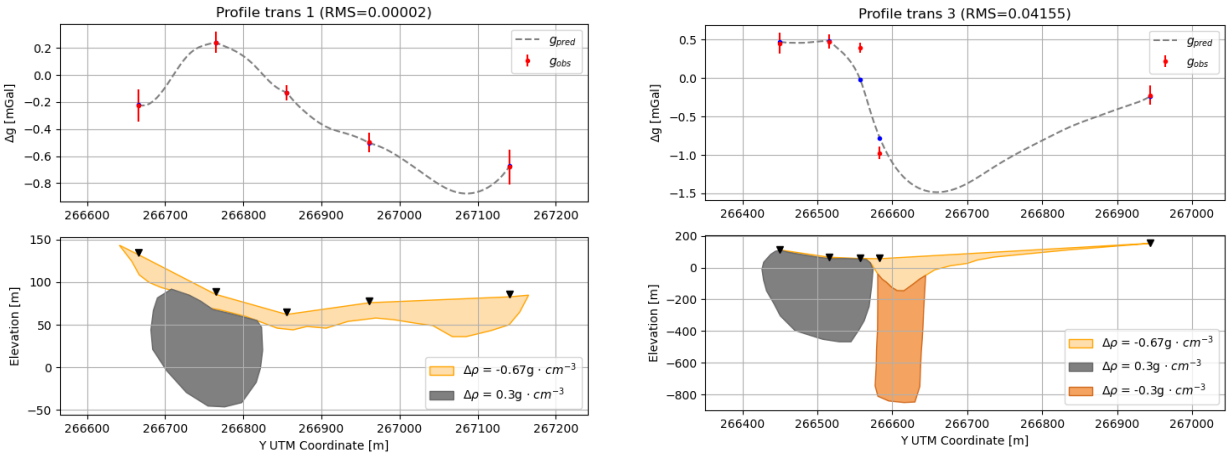

(a) Profile trans 1

(b) Profile trans 3

Figure A.2: Figure (a): Profile trans 1. Figure (b): Profile trans 3

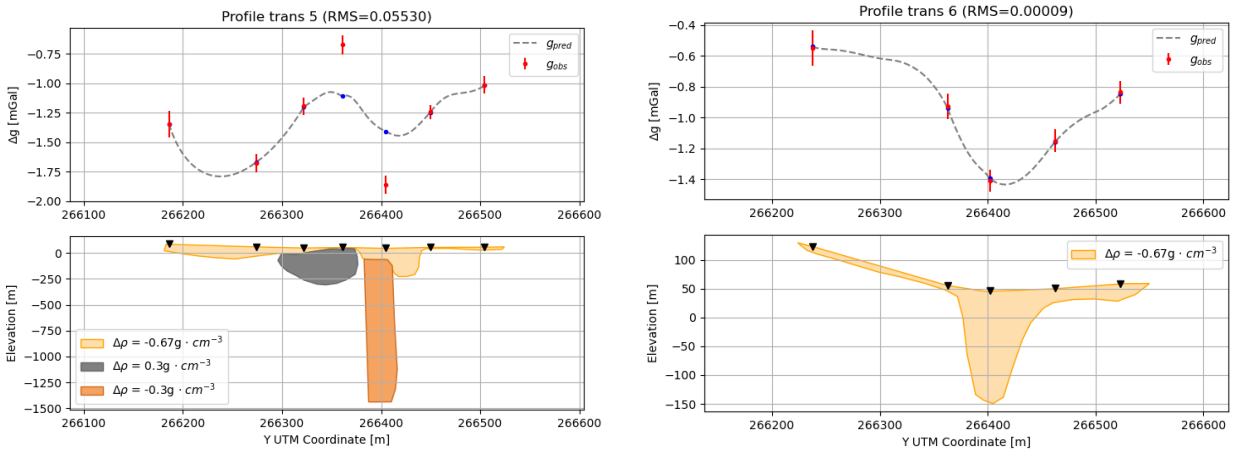

(a) Profile trans 1 (b) Profile trans 3

Figure A.3: Figure (a): Profile trans 5. Figure (b): Profile trans 6

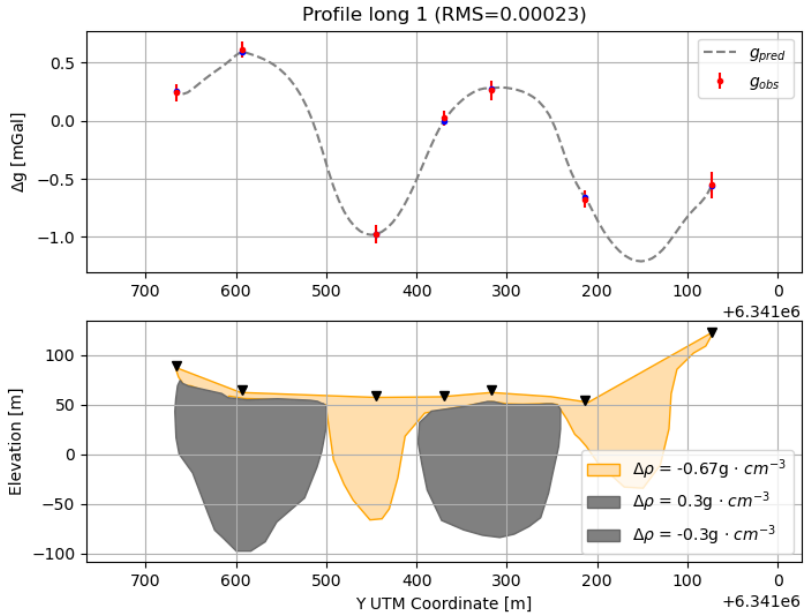

Figure A.4: Profile long 1

Annex B

Electric resistivity tomography

B.1. Measured apparent resistivities

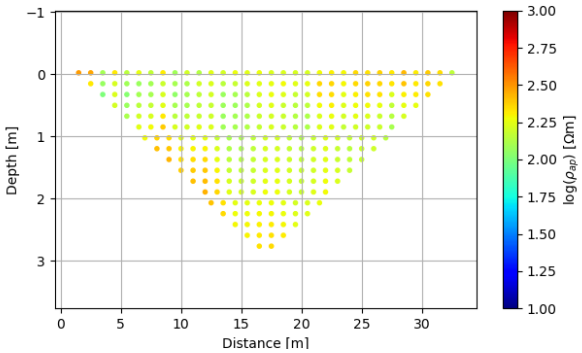

(a) Profile ERT 2

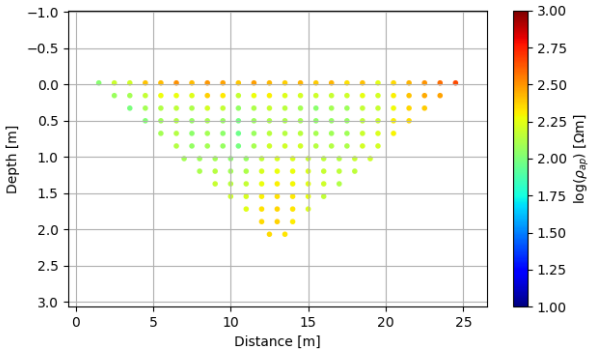

(b) Profile ERT 4

Figure B.1: Figure (a): Profile ERT 2. Figure (b): Profile ERT 4

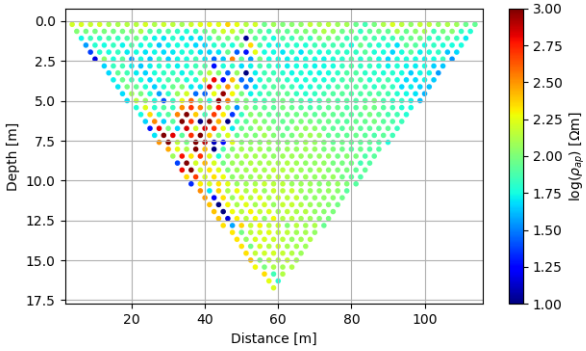

(a) Profile ERT 5

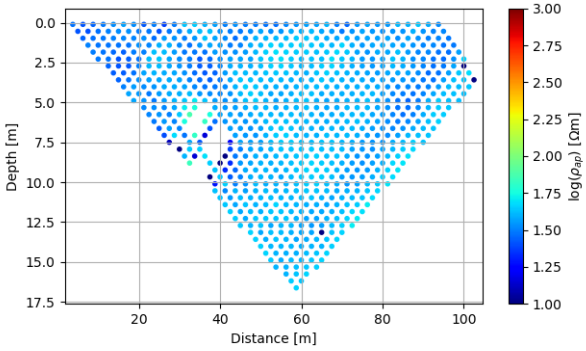

(b) Profile ERT 6

Figure B.2: Figure (a): Profile ERT 5. Figure (b): Profile ERT 6

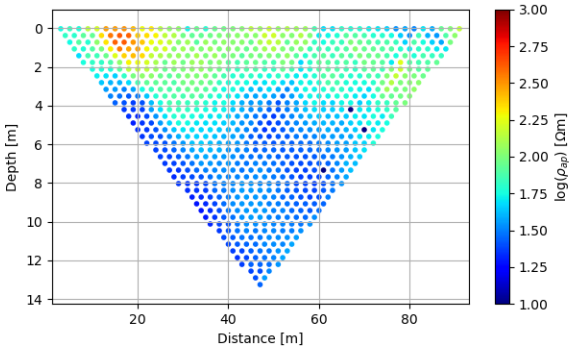

(a) Profile ERT 7

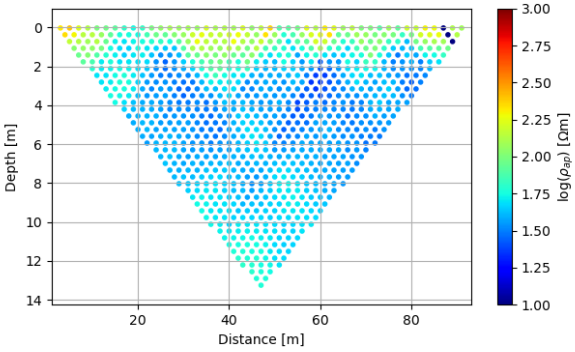

(b) Profile ERT 8

Figure B.3: Figure (a): Profile ERT 7. Figure (b): Profile ERT 8

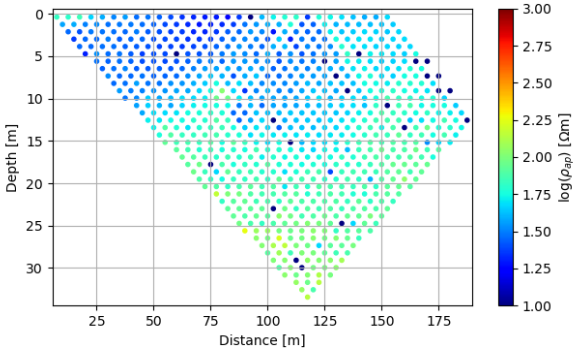

(a) Profile ERT 9

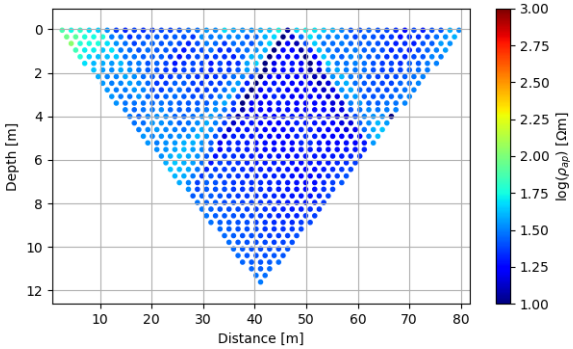

(b) Profile ERT 11

Figure B.4: Figure (a): Profile ERT 9. Figure (b): Profile ERT 11

B.2. Predicted apparent resistivities

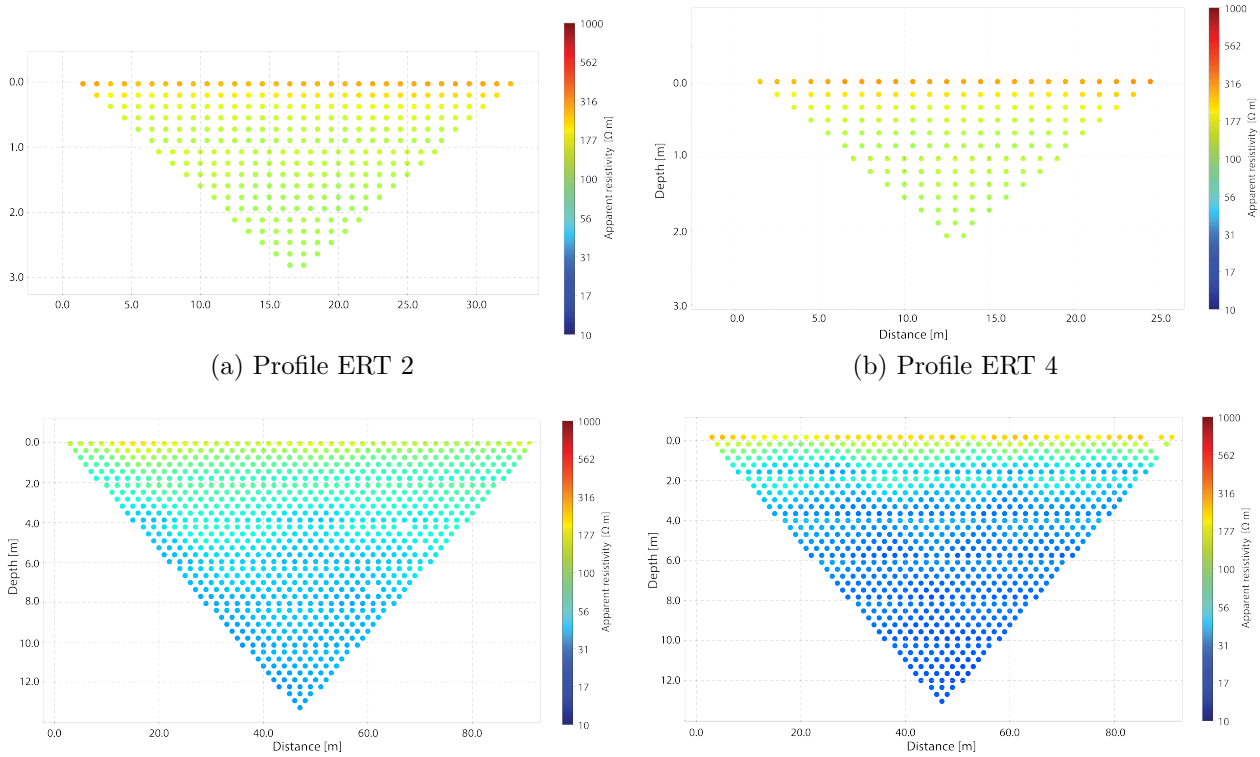

(a) Profile ERT 2

(b) Profile ERT 4

(c) Profile ERT 7

(d) Profile ERT 8

Figure B.5: Figure (a): Profile ERT 9. Figure (b): Profile ERT 11

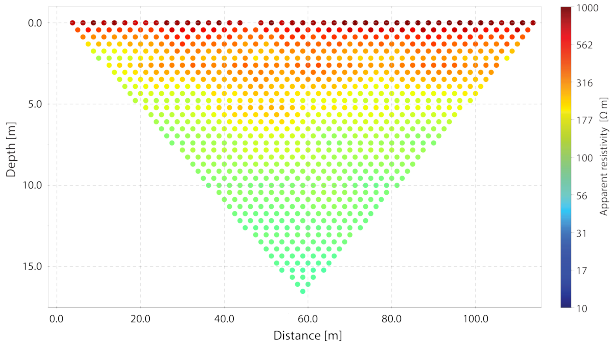

(a) Profile ERT 10

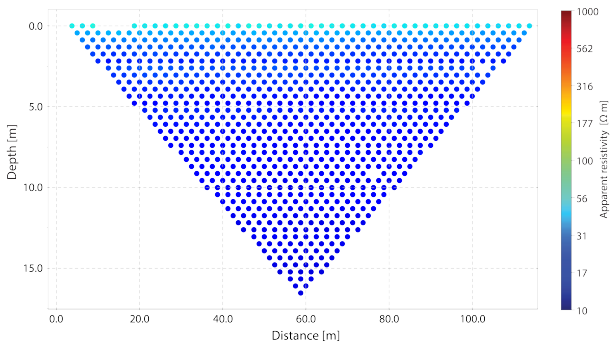

(b) Profile ERT 11

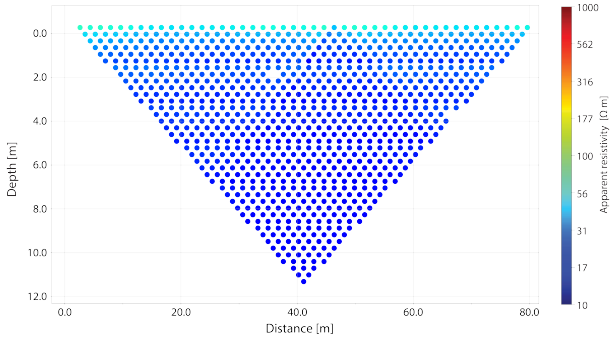

(c) Profile ERT 12

Figure B.6: Figure (a): Profile ERT 9. Figure (b): Profile ERT 11

B.3. Inverted resistivities

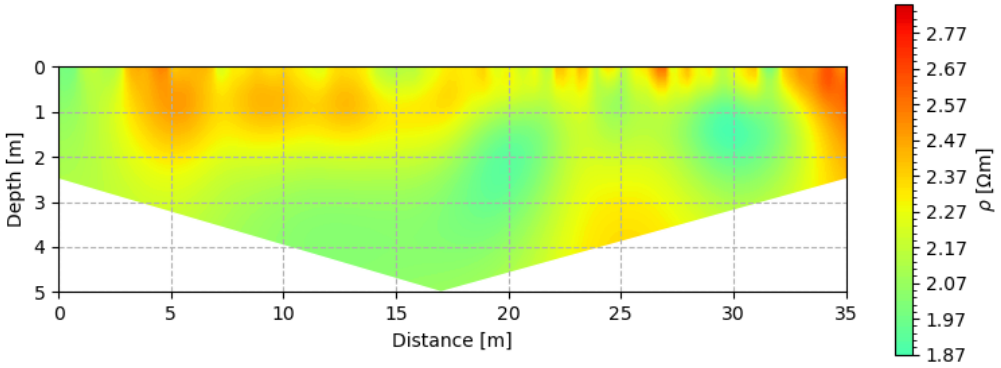

Figure B.7: Model of profile ERT 2. $rms = 0.4$

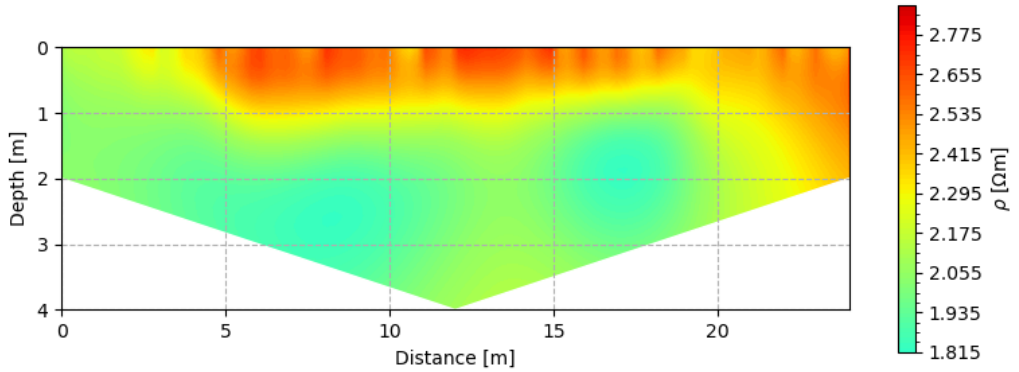

Figure B.8: Model of profile ERT 4. $rms = 0.37$

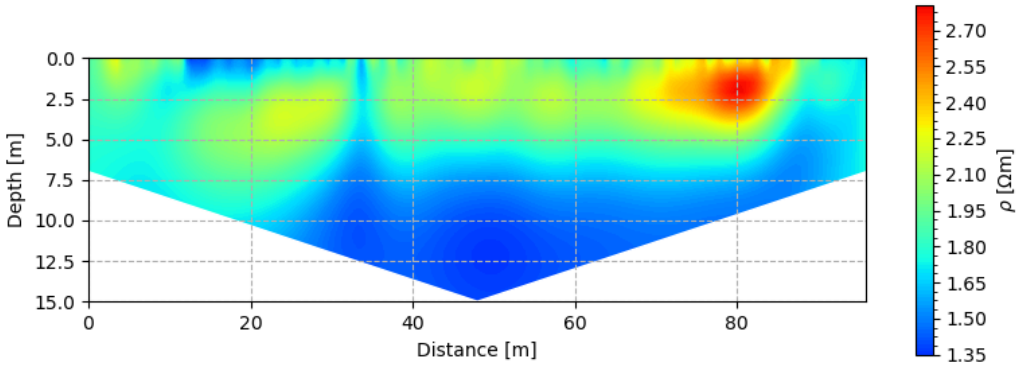

Figure B.9: Model of profile ERT 7. $rms = 0.32$

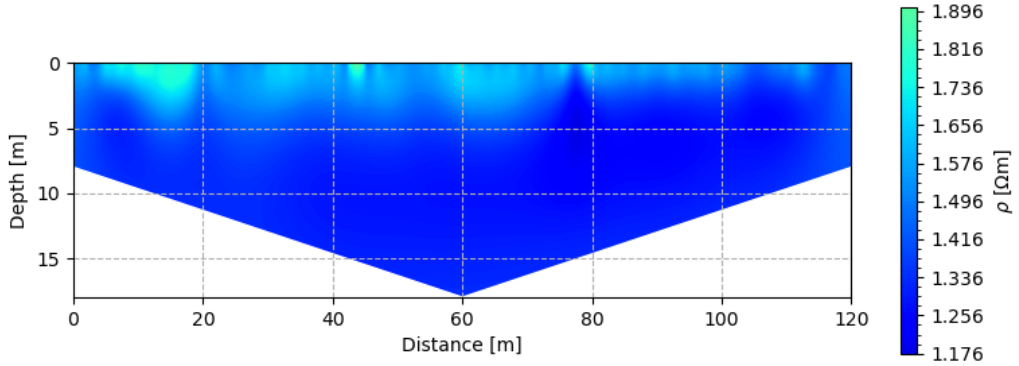

Figure B.10: Model of profile ERT 11

B.4. Water table depth estimation

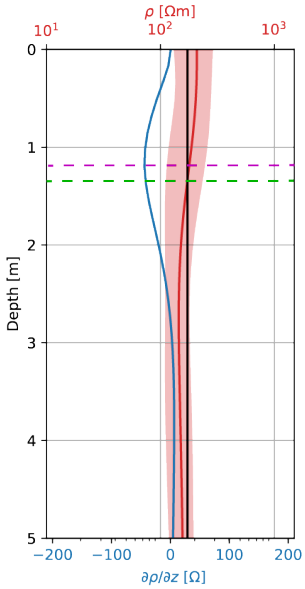

(a) 1D resistivity curve of profile ERT 2.

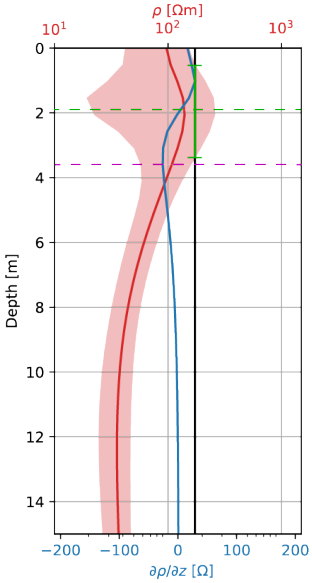

(b) 1D resistivity curve of profile ERT 7.

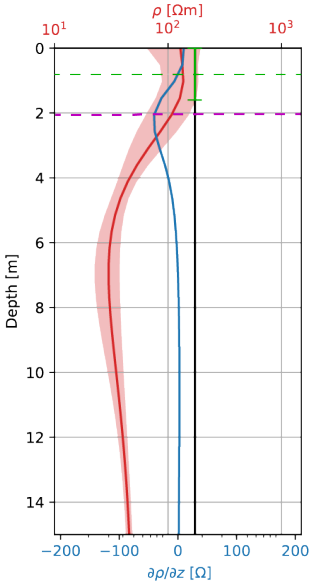

(c) 1D resistivity curve of profile ERT 8.

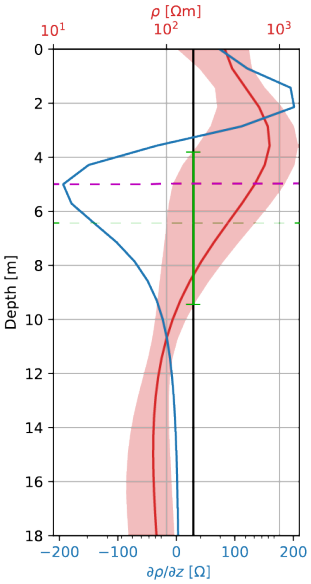

(d) 1D resistivity curve of profile ERT 10.

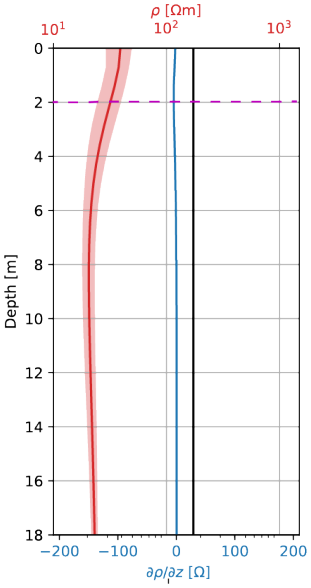

(e) 1D resistivity curve of profile ERT 11.

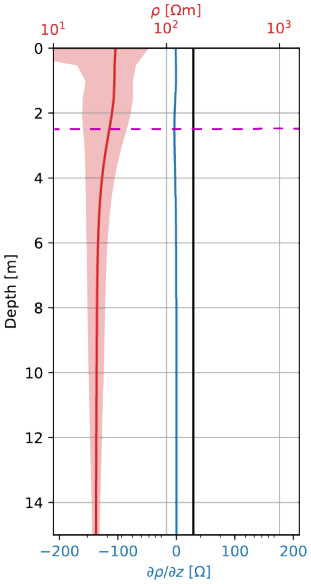

(f) 1D resistivity curve of profile ERT 12.

Figure B.11: 1D resistivity curves and water table depth estimation of profiles ERT 8, ERT 10, ERT 11 and ERT 12. The purple line corresponds to the water table depth based on the resistivity method, and the green line corresponds to the water table depth based on the gradient method

Annex C

Transient electromagnetic

C.1. Voltage measurements

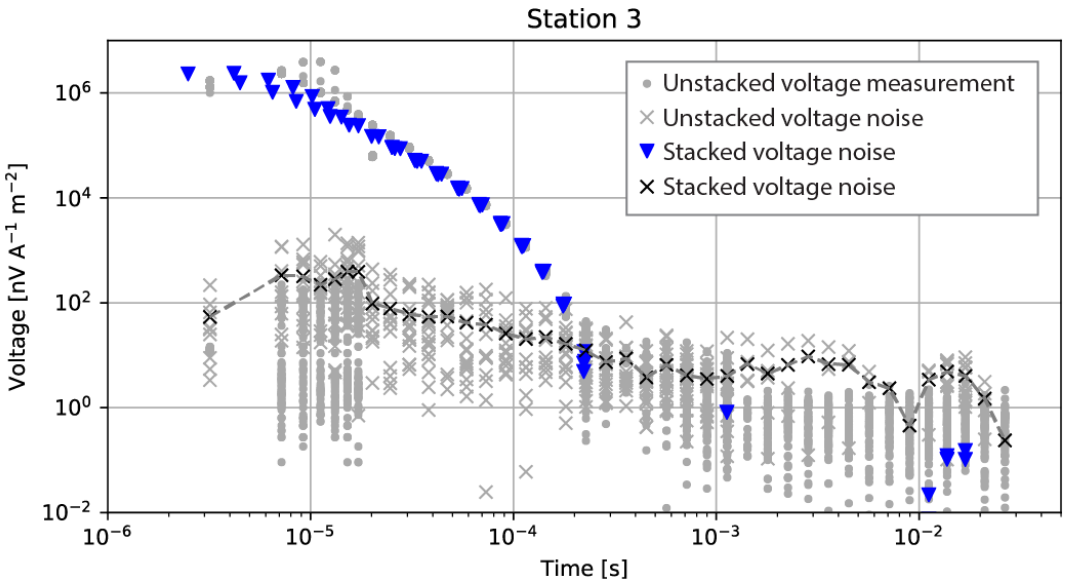

Figure C.1: Measured voltage of station TEM 3

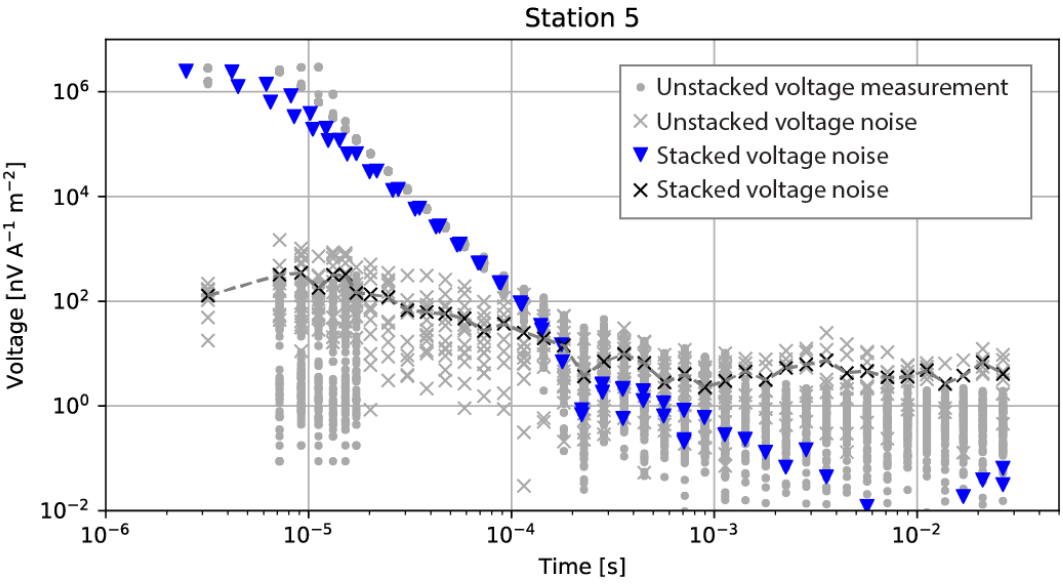

Figure C.2: Measured voltage of station TEM 5

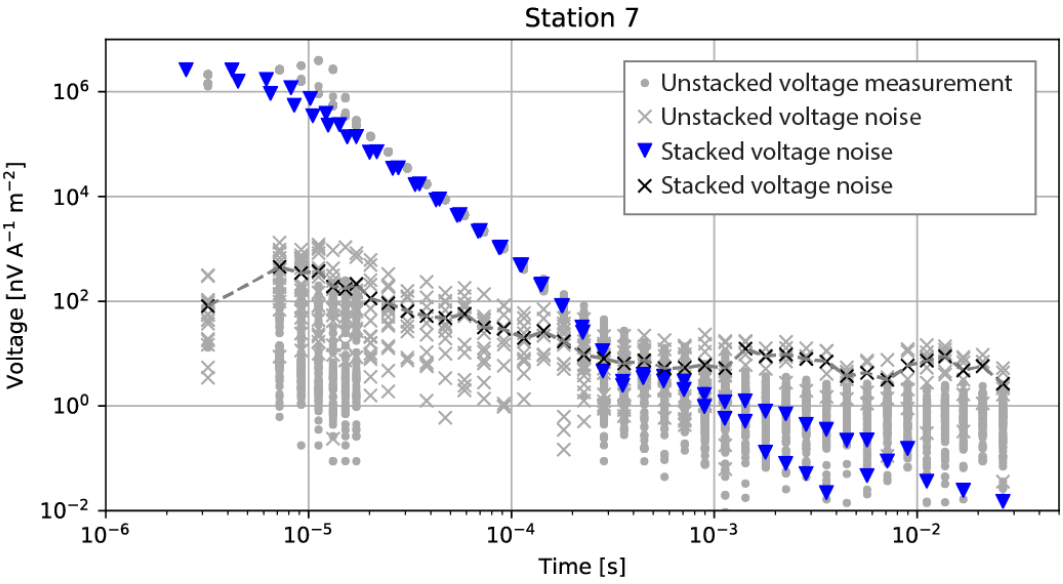

Figure C.3: Measured voltage of station TEM 7

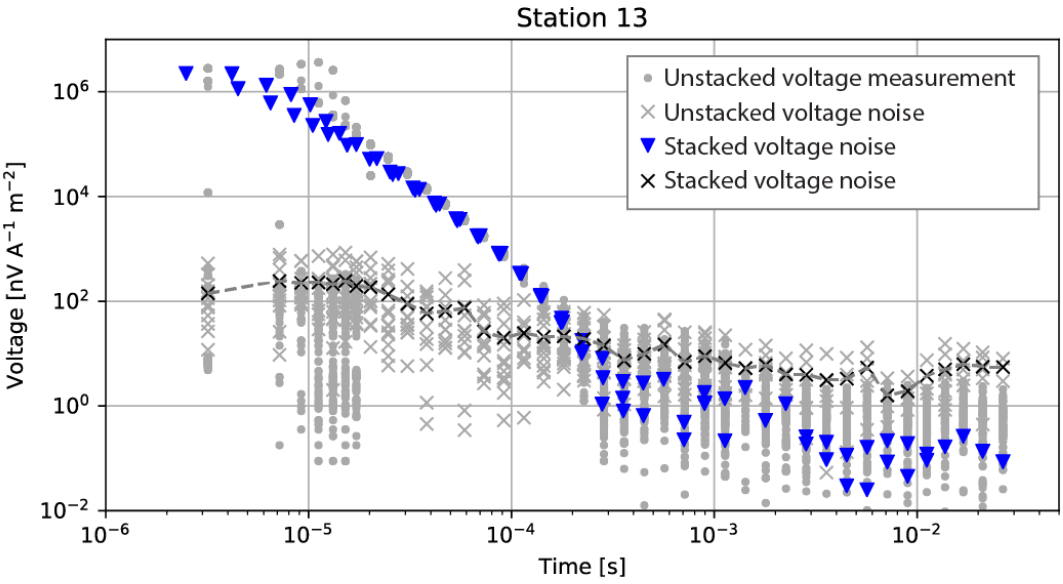

Figure C.4: Measured voltage of station TEM 13

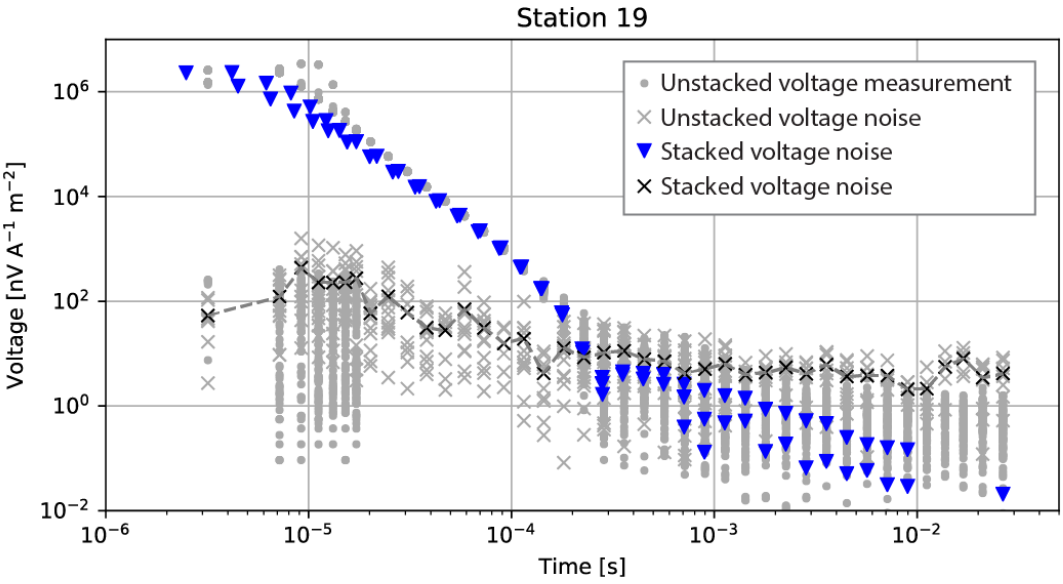

Figure C.5: Measured voltage of station TEM 19

C.2. Apparent resistivity and modelled resistivity

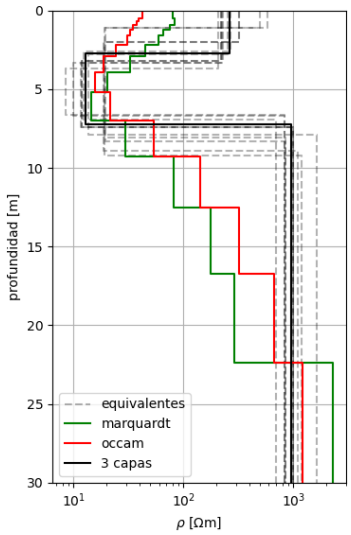

(a) Inverted resistivity models of station TEM 5

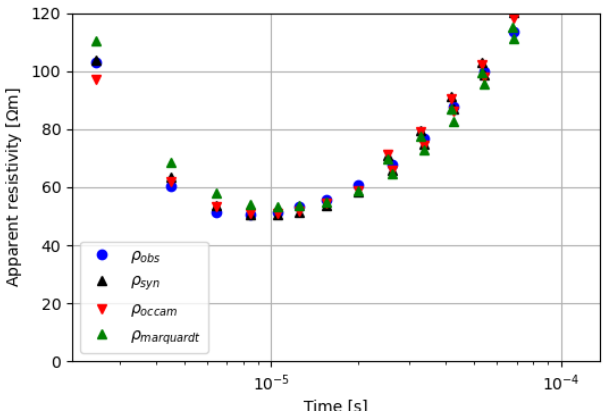

(b) Observed and modelled apparent resistivities of station TEM 5

Figure C.6: Observed and modeled apparent resistivity, and inverted resistivity of station TEM 5. $rms_{3-layer} = 0.053$, $rms_{occam} = 0.096$, $rms_{marquard} = 0.10$

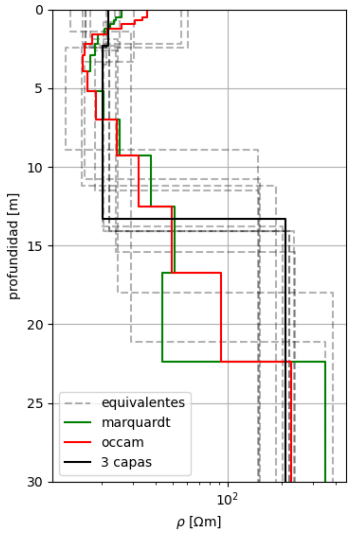

(a) Inverted resistivity models of station TEM 7

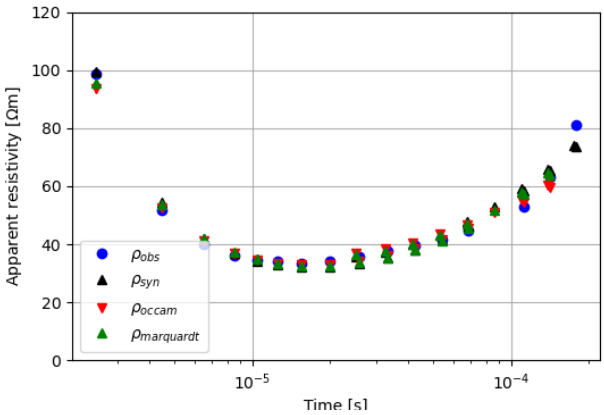

(b) Observed and modelled apparent resistivities of station TEM 7

Figure C.7: Observed and modeled apparent resistivity, and inverted resistivity of station TEM 7. $rms_{3-layer} = 0.086$, $rms_{occam} = 0.051$, $rms_{marquard} = 0.053$

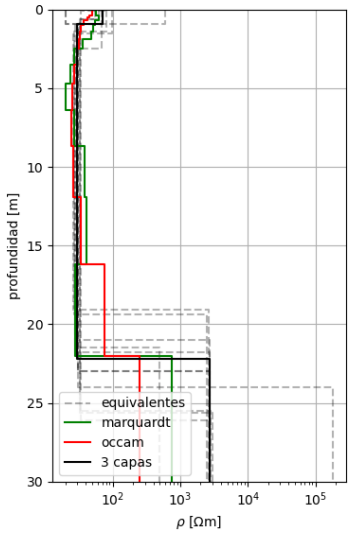

(a) Inverted resistivity models of station TEM 13

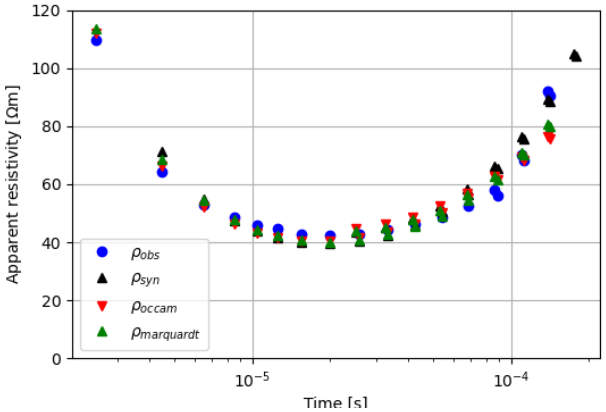

(b) Observed and modelled apparent resistivities of station TEM 13

Figure C.8: Observed and modeled apparent resistivity, and inverted resistivity of station TEM 13. $rms_{3-layer} = 0.081$, $rms_{occam} = 0.111$, $rms_{marquard} = 0.087$

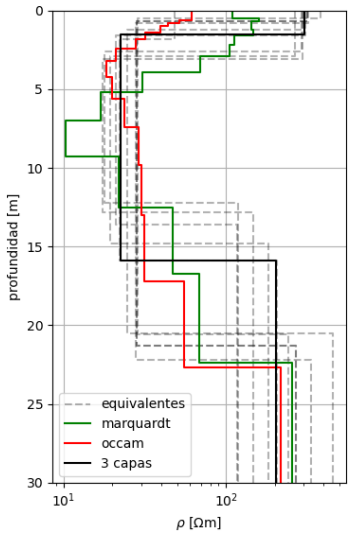

(a) Inverted resistivity models of station TEM 19

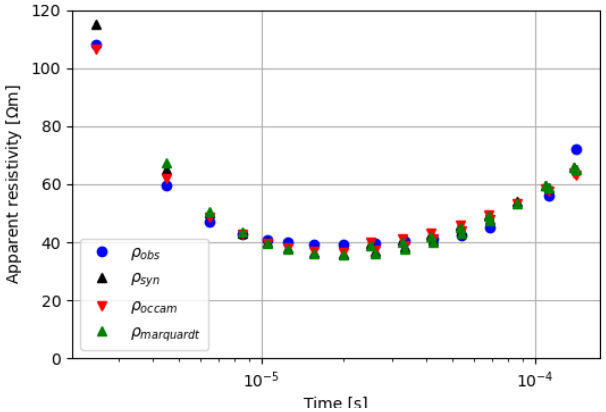

(b) Observed and modelled apparent resistivities of station TEM 19.

Figure C.9: Observed and modeled apparent resistivity, and inverted resistivity of station TEM 19. $rms_{3-layer} = 0.092$, $rms_{occam} = 0.096$, $rms_{marquard} = 0.101$

Annex D

Mapped and infered faults

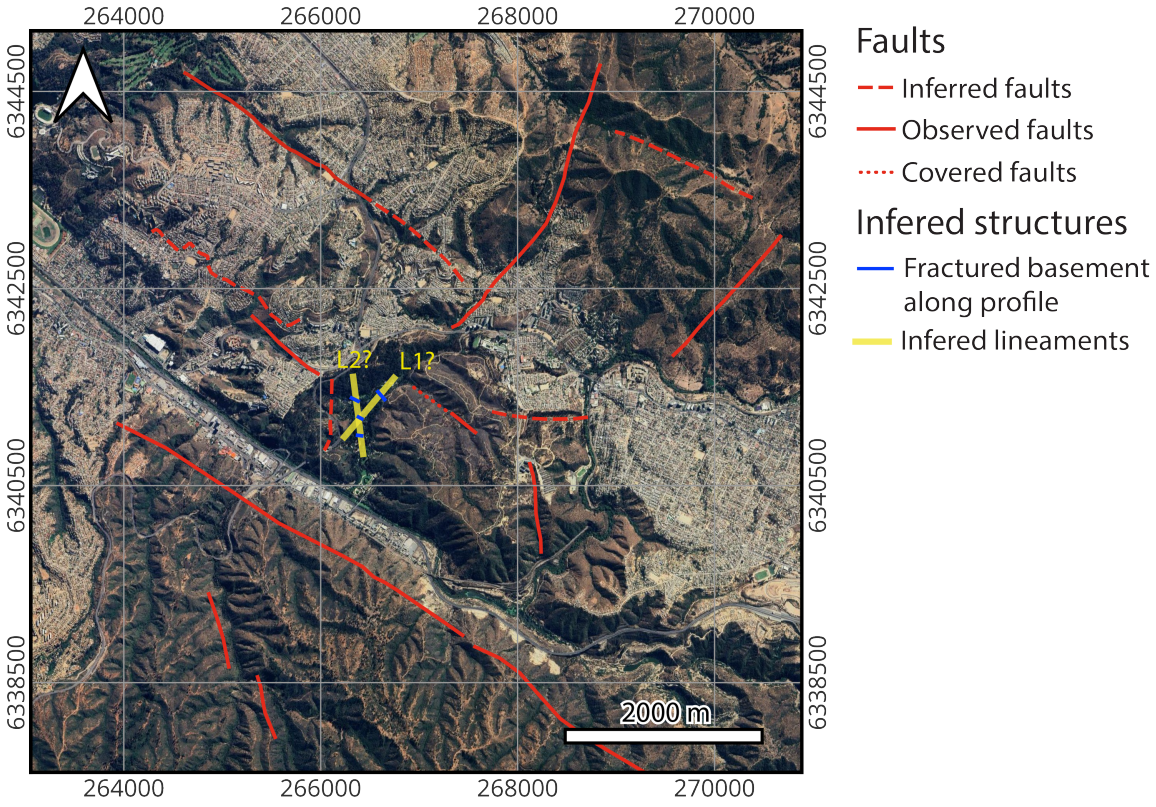

Figure D.1: Mapped and inferred faults from gravimetric measurements.